Lower-hybrid wave structures and interactions with electrons observed in magnetotail reconnection diffusion regions

Shan Wang[1,2], Li-Jen Chen[2], Naoki Bessho[1,2], Jonathan Ng[1,2], Michael Hesse[3], Daniel B. Graham[4], Olivia Le Contel[5], Daniel Gershman[2], and Barbara Giles[2]

[1]Astronomy Department, University of Maryland, College Park, MD, USA 20742

[2]NASA Goddard Space Flight Center, Greenbelt, MD, USA 20771

[3]NASA Ames Research Center, Mountain View, CA, USA 94043

[4]Swedish Institute of Space Physics, Uppsala SE-75121, Sweden

[5]Laboratoire de Physique des Plasmas, CNRS/Sorbonne Université/Université Paris-Saclay/Observatoire de Paris/ Ecole Polytechnique Institut Polytechnique de Paris, Paris, France

*swang90@umd.edu

Key points

- A dozen of magnetotail EDR with near-zero to 30% guide field are analyzed to establish lower-hybrid wave properties therein
- Electron temperature fluctuations due to electron acceleration and current sheet corrugation are correlated with the wave potential
- The electron pressure gradient contribution to the wave field and electron vortices correlated with field line twisting are demonstrated

Abstract

We investigate waves close to the lower-hybrid frequency in 12 magnetotail reconnection electron diffusion region (EDR) events with guide field levels of near-zero to 30%. In about half of the events, the wave vector has a small component along the current sheet normal, consistent with known lower-hybrid drift wave properties, but the perpendicular magnetic field fluctuations can be comparable or greater than the parallel component, a feature unique to the waves inside and adjacent to EDRs. Another new wave property is that the wave vector has a significant component along the current sheet normal in some events and completely along the normal for one event. In 1/4 of the events, the $\nabla \cdot \boldsymbol{P}_e$ term has a significant contribution to the wave electric field, possibly a feature of lower-hybrid waves more likely to exist in the diffusion region than further away from the X-line. Electron temperature variations are correlated with the wave potential, due to wave electric field acceleration and crossings at the corrugated separatrix region with different amounts of mixing between reconnection inflowing and outflowing populations. The latter also leads to the anti-correlation between parallel and perpendicular temperature components. Using four-spacecraft measurements, the magnetic field line twisting is demonstrated by the correlated fluctuations in $(\nabla \times \boldsymbol{V}_{E\times B})_{||}$ and $(\nabla \times \mathbf{B})_{||}$. The lower-hybrid wave in the EDR of weak guide field reconnection may be generated near separatrices and penetrate to the mid-plane or locally generated, and the latter possibility is beyond the prediction of previous reconnection simulations.

1. Introduction

Lower-hybrid waves at frequencies between the ion and electron cyclotron frequencies are commonly observed in current sheets (e.g., Norgren et al., 2012; Graham et al., 2019). One possible wave generation mechanism is the lower-hybrid drift instability (e.g., Davidson et al., 1977), where a pressure gradient exists along the current sheet normal direction. Ions are mostly demagnetized. In the spacecraft or current sheet frame, the ion diamagnetic drift has comparable amplitudes and an opposite sign with the $\boldsymbol{E} \times \boldsymbol{B}$ drift. Electrons mostly follow the $\boldsymbol{E} \times \boldsymbol{B}$ drift with modifications from the electron diamagnetic drift. The corresponding waves have near-perpendicular propagation with respect to the magnetic field. The wave that often develops at the boundary of the current sheets is mostly electrostatic, though the electron $\boldsymbol{E} \times \boldsymbol{B}$ current induces non-zero magnetic field fluctuations (Norgren et al., 2012). The wavelength is relatively short with $k_\perp \rho_e \sim 1$, where ρ_e is the electron thermal gyro-radius. The short-wavelength mode is shown to be suppressed in the current sheet center, where a long-wavelength mode with $k_\perp \sqrt{\rho_i \rho_e} \sim 1$ develops, where ρ_i is the ion thermal gyro-radius (Daughton, 2003). The long-wavelength mode tends to be more electromagnetic than the short-wavelength mode. In addition to the lower-hybrid drift instability, the relative drift between two ion populations (Graham et al., 2017) or between ions and electrons (Graham et al., 2019) without the effect of the pressure gradient can also induce lower-hybrid waves.

The lower-hybrid wave that develops in regions with a strong magnetic field and low plasma β is typically the short-wavelength mode, in which the wave number $k\rho_e$ is a fraction of unity. Examples include waves at the boundary of the current sheet (e.g., Norgren et al., 2012; Zhou et al., 2009; Le Contel et al., 2017), in the separatrix region of magnetic reconnection far away from the electron diffusion region (EDR) (the satellite does not encounter the EDR during the current sheet crossing) at the magnetotail (e.g., Holmes et al., 2021), at dayside magnetopause on the magnetospheric side (Graham et al., 2019), and at dayside magnetopause on the magnetosheath side (Tang et al., 2020). The wave propagates mainly in the L-M plane roughly perpendicular to the magnetic field, where L is along the reversing magnetic field direction, N is along the current sheet normal, and M is along the current direction to form the right-hand orthogonal LMN coordinate system. The magnetic field fluctuation is mainly along the background magnetic field at boundary layers with large amplitudes of the magnetic field (e.g., Zhou et al., 2009).

In the short-wavelength mode wave, the electron bulk motion mostly follows the $\boldsymbol{E}\times\boldsymbol{B}$ drift, and the diamagnetic drift provides limited modifications, such as the case in the separatrix region of a particle-in-cell simulation of symmetric reconnection with zero guide field (Wang et al., 2021a). Electron vortices in the background flow frame develop in the short-wavelength mode wave, due to the $\boldsymbol{E}\times\boldsymbol{B}$ drift associated with the alternating diverging and converging electric fields (e.g., Chen et al., 2020; Ng et al., 2020). In the zero guide field simulation, the long-wavelength mode wave develops at the X-line, where electrons perform the demagnetized meandering motion not following the $\boldsymbol{E}\times\boldsymbol{B}$ drift (Wang et al., 2021a). In observations, deviations between the electron bulk velocity and the $\boldsymbol{E} \times \boldsymbol{B}$ drift are observed, but usually the $\boldsymbol{E} \times \boldsymbol{B}$ drift is able to account for most of the electron bulk velocity, including the fluctuations in the wave (e.g., Graham et al., 2017, 2019; Holmes et al., 2021).

Electron vortices in the short-wavelength mode wave have comparable scales with the electron gyro-radius; consequently, electrons are accelerated/decelerated by the wave potential, leading to temperature variations, e.g., discussed in the EDR observation (Chen et al., 2020) and in a particle-in-cell simulation study of symmetric reconnection (Wang et al., 2021a). The vortices are also associated with twisting of the field lines, which may potentially change the magnetic field connectivity and lead to secondary reconnection. Such a picture was discussed based on observations at the dayside magnetopause (e.g., Ergun et al., 2019) and magnetotail (Chen et al., 2020). The field line twisting was later examined in the simulation by plotting the perpendicular magnetic field patterns and tracing field lines (Wang et al., 2021a), as well as in magnetotail observations by reconstructed magnetic field structures (Holmes et al., 2021).

For the magnetotail, lower-hybrid waves are reported in two EDRs. Chen et al. (2020) reported lower-hybrid waves inside the EDR in the electron outflow jet for an event with a guide field of ~30% of the reconnecting component. The wave propagates mainly perpendicular to the background field in the L-M plane, which is mainly along the outflow direction in this case. The electron gyro-scale vortices lead to preferential perpendicular heating with nongyrotropic distribution functions. Cozzani et al. (2021) studied lower-hybrid waves observed in an event with a guide field of ~13%. The wave extends from the EDR to the separatrix region outside, the electric field has electron-scale gradients, and the wave has a significant electromagnetic component. Lower-hybrid waves in EDRs with lower guide field than 10%~20% have not been reported in observations, and it is not clear whether all lower-hybrid fluctuations close to the EDR exhibit similar properties. We are thus motivated to conduct a survey to first identify all magnetotail EDRs, and then perform analysis of lower-hybrid waves inside and adjacent to the EDRs.

In this paper, we report properties of lower-hybrid wave (defined as waves close to the lower-hybrid frequency) in 12 reconnection EDR crossings in the magnetotail during the Magnetospheric Multiscale (MMS) mission in 2017-2020. The EDR events are identified by features that V_{ix} (in GSM) has reversals or changes from above a few hundred km/s to near-zero values, while V_e (especially along Y_{GSM}) has a much larger amplitude than V_i. In each event, the ion bulk motion is small and far from the $\boldsymbol{E} \times \boldsymbol{B}$ drift; the large-amplitude electron flow along the M direction supports the current sheet, and the L component of the velocity is significant with deviations from the $\boldsymbol{E} \times \boldsymbol{B}$ drift (by more than 30%) close to the mid-plane. The Hall electric field E_N exists and mostly points towards the current sheet mid-plane, though the E_N reversal may not occur exactly at the current sheet mid-plane due to the guide field effect. We have also confirmed that nongyrotropic electron distributions exist during the current sheet crossing. Thus, at least part of each crossing can be considered as the EDR, and the satellite remains close to the EDR, though it may not be exactly inside the EDR during the entire crossing. We survey the EDR events using data from MMS 1. The spacecraft separation is typically 20~40 km, and the electron inertia length (d_e) corresponding to a density of 0.01~1 cm^{-3} is 5~50 km.

Thus, the spacecraft separation is a few d_e, comparable to the thickness of the electron current layer, and usually all four spacecraft cross the EDR with similar features. The wave properties we examine are: whether electrons follow the $\boldsymbol{E} \times \boldsymbol{B}$ drift in the wave field, whether the electron temperature is modulated, and whether magnetic field line twisting features exist in the lower-hybrid vortices.

2. Data

The observational data are from the MMS measurements in the burst mode. The magnetic fields are from the Flux Gate Magnetometer (FGM) at 128 samples/s (Russell et al., 2016) and Search Coil Magnetotail (SCM) at 8192 samples/s (Le Contell et al., 2016). Electric fields are from the double probes at 8192 samples/s (Ergun et al., 2016; Lindqvist et al., 2016; Torbert et al., 2016). Plasma data are from the Fast Plasma Investigation (FPI), where the ion measurements have the time resolution of 0.15 s, and electron measurements have the time resolution of 0.03 s. The electron moments are from the 'partial moments' data files, where only data in energy channels above a certain threshold are used in the moments calculation, to avoid spurious numbers related to uncertainties such as in the process of photo-electron removal at lower energies. The lower energy limit is selected by requiring the densities to be positive, and the electron speed to be lower than 3×10^4 km/s. A typical lower energy limit is 10~30 eV, while for low-density events, the lower-energy limit can be up to 100 eV. We have confirmed that the agreement between the electron perpendicular velocity and the $E \times B$ drift outside of the EDR justifies the validity of using the partial moments data.

The events analyzed in this study are listed in Table 1. The intervals are for the wave property analysis. The first twelve events are waves inside the current sheet approaching the mid-plane. The last four events are wave packets near the separatrix with a large magnetic field, to be compared with those penetrating all the way to the mid-plane. These four events belong to the same current sheet with one of the above twelve events, but the wave packet is clearly separate from the wave near the mid-plane. They are still inside the ion diffusion region, judged by the clear Hall electric field, small ion outflow speed, and clear deviation of the ion perpendicular velocity from the $\boldsymbol{E} \times \boldsymbol{B}$ drift. The guide field is estimated using $|B_M|$ either at the B_L reversal or at the asymptotic B_L region, divided by the asymptotic B_L. For the guide field level lower than 10%, we may just consider the guide field to be small, as the exact guide field level is uncertain due to B_M variations. In the following sections, we will analyze the wave properties, the electron force balance, electron heating, and field line twisting, in order to establish general properties of lower-hybrid waves in magnetotail reconnection diffusion regions.

We also present the electron bulk velocity along L from a 2D and a 3D particle-in-cell simulation using the VPIC code (Bowers et al., 2008). The 2D simulation has a guide field level of 10%, and data are just used for illustrating the spacecraft trajectories. The 3D simulation has zero guide field, where lower-hybrid waves develop with a dominant propagation along the M direction. The 2D simulation is in the L-N plane and does not allow for the variation along M, so lower-hybrid waves do not develop. The wave structures in this simulation are investigated in detail and published in Wang et al.

(2021a), and some key results are mentioned in section 1. The plot of the 3D simulation data is used to illustrate where lower-hybrid waves are present in section 7.

3. Wave properties

We will examine the ratio between the electric and magnetic wave fields in wave power spectrograms, the dominant wave field components, and the wavenumber and propagation directions.

3.1 Properties consistent with known lower-hybrid waves

3.1.1 L-M plane propagation with dominant B_L fluctuations

An electron current layer is encountered on 2018-08-27 around 12:15:43 UT (Figure 1, No.10 in Table 1), where the wave properties are consistent with the known lower-hybrid waves. During a longer interval of about 2 min, the GSM x component of V_i reverses from negative to positive values (not shown), indicating a transition from the tailward to Earthward (along the +L ~ +x direction) of a reconnection X-line. The interval shown in Figure 1 has $V_{eL} << V_{iL} < 0$, and a large-amplitude negative V_{eM} associated with the bipolar E_N, demonstrating the location to be in the diffusion region. A clear deviation between $V_{e\perp L}$ and $V_{E\times B,L}$ exists during 12:15:42.8-12:15:43.8 UT, while the agreement between the two is relatively good at other time, which suggests that the spacecraft crossed the demagnetized electron outflow jet. The lower-hybrid wave power at around f_{lh} (Figures 1f-1g) is strong throughout the interval, and is particularly enhanced at f_{lh} to $f_{ce}/2$ around 12:15:41.3-12:15:42.7 UT (clearest if starting from 12:15:41.9 UT). During this time the B_L amplitude is large and nongyrotropic electron distributions exist (Figure 10), indicating that MMS1 is close to the separatrix while electrons are not completely magnetized. MMS4 measures B_L~0 (Figure 2b), and $V_{E\times B,L}$ filtered at below 1 Hz is up to -9000 km/s (not shown), similar to but with a larger amplitude than that from MMS1 later near the mid-plane (-6000 km/s). Therefore, the spacecraft stayed within the electron outflow jet of the EDR during 12:15:41.3-12:15:42.7 UT, and we will analyze the wave properties during this interval. The trajectory is illustrated with a black arrow in Figure 1h on top of the V_{eL} profile of a 2D particle-in-cell simulation of symmetric reconnection with the 10% guide field, which is just for the illustration purpose.

The wave property analysis is shown in Figure 2. A peak of the wave power is around 3-11 Hz, slightly above f_{lh} (0.5-3.3 Hz during the interval with an average of 1.9 Hz). The magnetic field variation is dominant in B_L, mainly parallel to the background magnetic field, and E_N dominates the electric field variation, consistent with the typical lower-hybrid drift wave features.

The wave penetrates to the close vicinity of the current layer mid-plane, as seen from B_L of four spacecraft (Figure 2b). B_L at MMS 4 reverses the sign during the wave interval, where fluctuations exist most of the time, except for a plateau right at B_L=0.

The wave propagation is determined using two methods, and the first one is based on the wavelet phase correlation between the measurements of four spacecraft. We obtain the Morlet wavelet transformation as a function of time and frequency for B_L at each spacecraft, and calculate the phase difference ($\Delta\Psi_{t,f,j1}$) for MMS-j (j=2,3,4) relative to MMS1 using the phase angle of the cross spectrum (e.g., equations 1-2 described in

Graham et al. (2016)). The phase difference is then translated to the time lag as $\Delta t_j = \Delta\Psi_{t,f,j1}/(2\pi f)$. With the time lag and the relative spacecraft positions, we cancalculate the amplitude and direction of the phase velocity at each time and frequency in the same way with the typical timing analysis (Harvey, 1998). Figures 2c-2f show the result at the selected frequency range of 5-11 Hz, where the red-blue curves represent increasing frequencies. During the marked interval of 12:15:41.3-12:15:42.7 UT, it shows relatively steady amplitudes and directions of $\mathbf{V}_{ph}$. The average direction over all the shown frequencies over the marked interval is [-0.318, -0.911, -0.262] LMN. The phase speed for the shown frequency range varies in the range of 3000-4000 km/s with an average of 3413 km/s. The wave propagation is mainly along the -M direction, and the significant E_N fluctuation is an indication of the formation of electron vortices with alternating diverging and converging electric fields in the M-N plane.

We also examine the importance of the electromagnetic component using $|\boldsymbol{E}|/(|\boldsymbol{B}|V_{ph})$ (magenta curve in Figure 2a) (e.g., Cozzani et al., 2021). For a pure electrostatic mode, the ratio goes to infinity. Using the above-deduced V_{ph} and taking the average value in the range of 5-11 Hz, $|\boldsymbol{E}|/(|\boldsymbol{B}|V_{ph})$ is about 4 for this event. Thus, a significant electromagnetic component exists.

The second method to determine the wave propagation is $\boldsymbol{k}(\omega) = i\mu_0\boldsymbol{J}(\omega) \times \boldsymbol{B}*(\omega)/|\boldsymbol{B}|^2$, based on Ampere's law (Bellan, 2016). The average magnetic field over four spacecraft and the current density from the curlometer method (Robert et al., 1998) are used for calculation. Figures 2g-2h show that the amplitude and direction of $\mathbf{k}$ is relatively steady at 5-11 Hz. The average **k** over this frequency range is 0.017×[-0.344, -0.853, -0.393] LMN km^{-1}. The standard deviation of the amplitude and direction of **k** over the selected frequency range is σ_k=0.006×[0.16,0.09,0.28] km^{-1}, and the standard deviation of angles between each pair of the **k** direction for different frequency bins is $\sigma_{\hat{k}}$=14°. During the wave interval, the minimum ρ_e at the maximum |**B**| is 29 km, so that $k\rho_e = 0.49$. We use the minimum ρ_e because the wave penetrates to the current layer mid-plane where ρ_e diverges, and the 3D particle-in-cell simulation analyzed in Wang et al. (2021a) suggests that lower-hybrid wave tends to develop off the mid-plane at the density gradient and gradually penetrates to the mid-plane (details not shown). Using the k values at each frequency bin in the 5-11 Hz frequency range, the corresponding V_{ph} is 2033~5685 km/s, roughly consistent with the wavelet correlation method. The difference of the **k** directions between the two methods is also small (8°). Therefore, we consider the wave propagation property of this event as being reliably determined. The $\boldsymbol{J} \times \boldsymbol{B}$ method shows rather consistent results at different frequencies, while the wavelet method still shows moderate variations in k_N and V_{ph}. The standard deviation of k_N is 0.42, greater than the variation of **k** components from the $\boldsymbol{J} \times \boldsymbol{B}$ method. Thus, the $\boldsymbol{J} \times \boldsymbol{B}$ method is considered to be better and used in the follow-up analysis (e.g., calculating the wave potential)

For this event near the end of the electron outflow jet, the dominant B_L fluctuation mainly parallel to the background magnetic field, the dominant perpendicular propagation, and the wavenumber of $k\rho_e$ smaller than but not far from unity are consistent with the typical lower-hybrid drift wave in the electron current layer (e.g., Chen et al., 2020).

3.2 New wave properties

3.2.1 L-M plane propagation with dominant B_N fluctuations

The event on 2018-08-21 around 11:01:04 UT is likely a crossing of the central EDR (Figure 3, No. 8 in Table 1). The electron current layer has a large-amplitude negative V_{eM} across the B_L reversal, and V_{eL} and B_N also reverse the sign. When B_N reverses, B_L is positive and V_{eM} remains a large amplitude, indicating that the spacecraft stays within the electron current layer. The E_N Hall field clearly exists, while $V_{e\perp L}$ and $V_{e\perp M}$ exhibit deviations from the $\boldsymbol{E} \times \boldsymbol{B}$ drift in the current layer. Two separate wave packets exist: one packet is in the positive B_L region around 11:01:01 UT, likely near the separatrix (marked with '1'); the other is near the current layer mid-plane (marked with '2'). The MMS trajectories of the wave intervals are illustrated with black arrows in Figure 3h.

The properties of the wave near the mid-plane during 11:01:03.3-11:01:04.5 UT are analyzed as follows. From the plot for magnetic field components (Figure 3a), we can already see that the dominant fluctuating component is B_N, mainly perpendicular to the background magnetic field, unlike the first event on 2018-08-27, which has the dominant fluctuation in B_L. The 1D FFT power spectrum (Figure 4a) further shows the dominant B_N at 8~10 Hz. $|\boldsymbol{E}|/(|\boldsymbol{B}|V_{ph})$ is around 2, suggesting the presence of a significant electromagnetic component. The $\boldsymbol{J} \times \boldsymbol{B}$ method gives a good estimate of the wave number at 6-9 Hz, a frequency range with steady results, and the average $\mathbf{k}$ is $0.024\times[0.278, -0.953, -0.123]$ LMN km^{-1}. With the minimum ρ_e=25 km during the wave interval, $k\rho_e$=0.60. The corresponding V_{ph} at 6-9 Hz is 1428~1878 km/s. The wavelet phase correlation result is fine in providing a steady result of V_{ph} over 6-9 Hz, but the variation in k_L is significant. The average $\mathbf{V}_{ph}$ is 3715 km/s along [-0.503, -0.818, 0.279] LMN, with a standard deviation of σ_V =846 × [0.37,0.25,0.28]. The dominant -M component of propagation and V_{ph} not far from the $\boldsymbol{J} \times \boldsymbol{B}$ method result roughly provide a justification of the $\boldsymbol{J} \times \boldsymbol{B}$ method result. Although B_N that is mainly perpendicular to the background magnetic field dominates the fluctuation, the properties of the wave propagation as mainly along -M and the wave number amplitude of $k\rho_e$=0.60 are still consistent with the typical lower-hybrid drift wave.

The wave packet near the separatrix around 11:01:01 UT (No. 16 in Table 1) is mainly electrostatic, as seen from the large-amplitude electric field variation (Figure 3b) and the wave power spectrograms (Figures 3f-3g). $|\boldsymbol{E}|/(|\boldsymbol{B}|V_{ph})$ is about 12, so the electromagnetic contribution still exists but is less important than that closer to the current sheet mid-plane. The propagation determined by the $\boldsymbol{J} \times \boldsymbol{B}$ method is mainly along -M with $\mathbf{k}$=0.027×[-0.055, -0.997, -0.063] LMN km^{-1}, corresponding to $k\rho_e$=0.46 and V_{ph}=1094~1498 km/s. The result is justified by another method of determining $\mathbf{V}_{ph}$ by fitting the wave potential between the electric field and magnetic field measurements (Norgren et al., 2012), which gives $\mathbf{V}_{ph}$=1500×[-0.241, -0.924, 0.297] LMN km/s.

3.2.2 propagation mainly along N

The event on 2017-06-17 is an electron-only reconnection event (R. Wang et al., 2018), where the large negative V_{eM} supports the current layer, a significant V_{eL} outflow jet exists (Figure 5c, No. 1 in Table 1), while ions do not have variations in either the bulk velocity or the temperature (not shown).

Wave fluctuations around f_{lh} exist across the B_L reversal, and the trajectories of the wave interval are illustrated in Figure 5h. The magnetic field fluctuations are dominant in B_M, and the electric field fluctuations are dominant in E_N (Figure 6a). $|\boldsymbol{E}|/(|\boldsymbol{B}|V_{ph})$ is around 3, indicating the importance of the electromagnetic component. The $\boldsymbol{J} \times \boldsymbol{B}$ and the wavelet phase correlation analysis give consistent results that the wave mainly propagates along N away from the mid-plane, different from the expected propagation of lower-hybrid waves mainly in the L-M plane. The results are shown in Figure 6 and listed in Table 1. The propagation along N can also be judged by looking at the time delay in magnetic field measurements from four spacecraft (Figure 6b-6c). MMS 1 is away from the other spacecraft mainly along the N direction, as can be seen from the clear time delay in B_L (Figure 6b). From the B_M fluctuations (Figure 6c), MMS 1 is clearly lagged from the other 3 spacecraft at $B_L<0$ between the black vertical dashed lines, and ahead of other spacecraft at $B_L>0$ between the blue vertical dashed lines (e.g., around the dip marked by the black arrow). The time delay is consistent with the wave propagation along N away from the mid-plane.

One notable feature is that the current sheet normal direction determined from the Minimum Variance Analysis is [-0.286, 0.952, 0.110] GSM, mainly along Y_{GSM}. Using the Maximum Directional Derivative (MDD, Shi et al. (2005)) method with four-spacecraft measurements of the magnetic fields, we obtain the consistent normal direction mainly along Y_{GSM} that is steady during the current sheet crossing. One possibility is that the large-scale (with the wavelength of a few d_i) current sheet flapping, e.g., related to the kink mode with a wavelength of a few ion gyro-radii (e.g., Karimabadi et al., 2003;

Sergeev et al., 2003; Wang et al., 2019; Richard et al., 2021), leads to variations of the current sheet orientations. The lower-hybrid wave originally generated along the current direction propagates to locations with tilted current sheets and appears to propagate along the normal direction of the local current sheets.

3.2.3 comparable fluctuations in all magnetic components and L-M plane propagation

The event on 2017-07-26 is in the electron outflow jet, where $V_{e\perp L}$ deviates from $V_{E\times B,L}$ near the mid-plane (Figure 7, No. 6 in Table 1). Two separate wave packets exist at $B_L<0$ and across the B_L reversal (mainly on the $B_L>0$ side), respectively, illustrated by the black arrows in Figure 7h.

The wave packet across the mid-plane during 00:03:54-00:04:02 UT exhibits comparable fluctuations in all three components of the magnetic field (Figure 8a). The comparable fluctuations are further supported by the Minimum Variance Analysis of 5-8 Hz magnetic field, where the eigenvalue ratio between the maximum and the intermediate variance directions is 1.8 and the ratio between the intermediate and minimum variance directions is 1.5 (both are small). $|\boldsymbol{E}|/(|\boldsymbol{B}|V_{ph})$ is around 10. Neither of the two methods provides unambiguously results of the wave propagation, where the results exhibit significant variations across frequencies and times (Figures 8d-8i). Nevertheless, both methods do indicate a rough propagation direction with a positive L and negative M direction. For the $\boldsymbol{J}\times\boldsymbol{B}$ method, **k**=0.024×[0.663, -0.746, 0.067] LMN km^{-1} with a standard deviation of σ_k=0.017×[0.51,0.38,0.51] km^{-1} corresponding to $k\rho_e$=0.24 and V_{ph} at 512~4639km/s, where ρ_e=10 km is the minimum value during the interval. For the wavelet phase correlation method, the average $\mathbf{V}_{ph}$ is 1908×[0.669, -0.689, 0.277] LMN km/s and the standard deviation is σ_V=562×[0.34,0.26,0.24] km/s. Thus, although the magnetic field fluctuation amplitudes are comparable in all three components, there is still a dominant propagation direction.

Let us summarize the wave properties of the waves close to the lower-hybrid frequency. The wave propagation properties obtained from two methods are listed in Table 1. The two methods typically result in consistent results. As shown in the examples, results with the standard deviation of the **k** direction smaller than 0.3 and $\sigma_{\hat{k}}$ smaller than 20° are steady over frequencies and time in visual inspection (like event No. 10), while some events may have more significant scattering of the **k** direction (like event No. 6), though it still indicates a preferential direction of propagation. For the 12 EDR current sheet crossings, the waves all penetrate to the current layer mid-plane. $|\boldsymbol{E}|/(|\boldsymbol{B}|V_{ph})$ is in the range of 2~21, suggesting the presence of an electromagnetic component, while the electromagnetic component is rather significant for those with the value below 10, typically close to the current sheet mid-plane. The dominant wave propagation direction in 4 out of 12 events near the mid-plane is mainly in (within 20° from) the L-M plane ($|k_N|$<0.35) and mainly perpendicular to the background **B**, though the dominant magnetic field fluctuation is not always in B_L or B_M along the background **B**. The other events have a significant propagation component along the current sheet normal direction ($|k_N|$>0.35). One event has the propagation almost entirely along the N direction, while N is mainly along Y_{GSM}. For 4 events, a separate wave packet exists far from the mid-plane, possibly near the separatrix further downstream of the EDR. These events all have the propagation mainly in the L-M plane. For all the events, $k\rho_e$ is in the range of 0.1~1, which is similar to those reported in the previous observations mentioned in the introduction section. It may appear unexpected that waves with a significant electromagnetic component do not have $k\rho_e$ too much smaller than unity. We will discuss in section 7 that the normalization plays a role, so that the conventional 'short'- and 'long'-wavelength modes may not be well distinguished by the $k\rho_e$ value, but the contribution of the $\nabla \cdot \boldsymbol{P}_e$ term in the wave electric field may be a better diagnostic.

4. Electron force balance in the wave

We next examine the electron pressure balance to see whether the wave electric field is mainly supported by $-\boldsymbol{V_e} \times \boldsymbol{B}$ as expected for typical lower-hybrid waves. Figure 9 (left) shows the E_N balance for the 2018-08-27 event No. 10. The comparison at MMS1 (Figure 9b) shows a clear DC offset between E_N and $(-\boldsymbol{V_e} \times \boldsymbol{B})_N$ before 12:15:42.2 UT, while the agreement between the two is better later where the E_N amplitude is smaller. The offset indicates the contribution of non-ideal terms (possibly the $\nabla \cdot \boldsymbol{P}_e$ term) to the DC E_N. The fluctuations of E_N are together with those of $(-\boldsymbol{V_e} \times \boldsymbol{B})_N$. We further plot dE_N by subtracting the 1-s sliding average for MMS 1, 2, and 3 (Figures 9c-9e). The electric field measurement and $-\boldsymbol{V_e} \times \boldsymbol{B}$ mostly track with each other, while sometimes discrepancies exist, such as MMS1 at 12:15:42.0-12:15:42.2 UT. (The instrumental uncertainty of E_N is about 3 mV/m, smaller than the discrepancy.) Thus, we conclude that the wave field is dominated by $-\boldsymbol{V_e} \times \boldsymbol{B}$, while non-ideal terms like the $\nabla \cdot \boldsymbol{P}_e$ term provide modifications.

In contrast, the 2017-08-10 EDR event (Zhou et al., 2019, No. 7 in Table 1) (Figure 9 right) has a more significant contribution from $\nabla \cdot \boldsymbol{P}_e$. Waves are mainly at the B_L>0 side after 12:18:33. Figure 9g shows the analysis at the spacecraft barycenter (Harvey, 1998). The sum (green) of the $-\boldsymbol{V_e} \times \boldsymbol{B}$ (blue) and $\nabla \cdot \boldsymbol{P}_e$ terms (red) agrees well with the electric field measurement (black), indicating the reliability of the calculation. For the DC component, the $-\boldsymbol{V_e} \times \boldsymbol{B}$ and $\nabla \cdot \boldsymbol{P}_e$ terms have comparable amplitudes. For the fluctuations, the contribution mainly comes from the $\nabla \cdot \boldsymbol{P}_e$ term, while $-\boldsymbol{V_e} \times \boldsymbol{B}$ does not have many fluctuations. We further examine the comparison between E_N and $(-\boldsymbol{V_e} \times \boldsymbol{B})_N$ at each spacecraft. In the measurements of MMS3 and MMS4, and part of MMS1, $(-\boldsymbol{V_e} \times \boldsymbol{B})_N$ more or less tracks E_N. The most significant discrepancy occurs at MMS2, and such discrepancy is consistent with the four-spacecraft calculation result.

Table 1 lists whether the $\nabla \cdot \boldsymbol{P}_e$ term has a significant contribution to the lower-hybrid wave field. For the events where measurements from four spacecraft are available, the $\nabla \cdot \boldsymbol{P}_e$ term is considered to be significant if the four-spacecraft calculation of the $\nabla \cdot \boldsymbol{P}_e$ term has comparable or dominant fluctuation levels with $-\boldsymbol{V_e} \times \boldsymbol{B}$ (marked by 'Y' in the table). For events with only available measurements at three spacecraft, the $\nabla \cdot \boldsymbol{P}_e$ term is considered to be significant if the difference between the fluctuation levels of E_N and $(-\boldsymbol{V_e} \times \boldsymbol{B})_N$ is comparable to the fluctuation amplitude of $(-\boldsymbol{V_e} \times \boldsymbol{B})_N$ like Figure 9i (marked by 'y' in the table). There are 4 out of 16 events where the $\nabla \cdot \boldsymbol{P}_e$ term has a significant contribution.

5. Electron temperature modulation

The electron temperature is expected to be modulated in the lower-hybrid wave since the wavelength ($k\rho_e$ of 0.1~1) is not significantly greater than ρ_e. We investigate the electron heating by examining the correlation between T_e and the wave potential $\phi = \int E_k V_{ph} dt$, where E_k is the bandpass electric field along the optimized **k** direction. For the typical lower-hybrid drift wave, the perpendicular current fluctuation is mainly contributed by the electron $\boldsymbol{E} \times \boldsymbol{B}$ drift, which is associated with $B_{||}$ fluctuations according to the Faraday's law, and it results in $\phi \propto dB_{||}$ (e.g., Norgren et al., 2012), so we also look at $dB_{||}$ patterns.

Figure 10 shows the result for the 2018-08-27 event No. 10 measured at MMS1. Correlated fluctuations exist in $dB_{||}$, ϕ, and T_e, but sometimes there are phase offsets, and $T_{e\parallel}$ and $T_{e\perp}$ components are not always varying together. The correlation coefficient between ϕ and total T_e during the shown interval is 0.59. The pure expected effect of ϕ in modulating T_e is through inflating and compressing the velocity distributions, as particles are accelerated and decelerated through the potential. If $\boldsymbol{k}$ is exactly perpendicular to the background magnetic field, ϕ only modulates $T_{e\perp}$ with a positive correlation. As $\boldsymbol{k}$ has a small difference from the perpendicular direction, electrons can be accelerated/decelerated along both parallel and perpendicular directions, so that both $T_{e\parallel}$ and $T_{e\perp}$ are modulated with ϕ with the same phase relationship (e.g., shown in Wang et al. (2021a)). The $v_{||}$ and $v_{\perp 2}$ spectrograms indeed show inflations and compressions along with the variations of v_{th} (overplotted black curves), where $v_{\perp 2}$ is along the local $\boldsymbol{B} \times (\boldsymbol{E} \times \boldsymbol{B})$ direction. For example, the $v_{||}$ spectrogram has a local minimum extension of the yellow-colored part at location 5, collocating with the local $T_{e||}$ minimum; the $v_{\perp 2}$

spectrogram has a local minimum extension of the yellow-colored part as well as a minimum $T_{e\perp}$ at location 4. The 2D reduced distributions in the $v_{||} - v_{\perp 1}$ plane at six selected locations are shown on the right, where $v_{\perp 1}$ is along the local $\boldsymbol{E} \times \boldsymbol{B}$ direction. The inflation in the perpendicular plane can also be seen in distributions 5 and 6, where the contour between the yellow and green colors is expanded (e.g., from ~3×10^4 to ~3.5×10^4 km/s along the positive $v_{\perp 2}$ direction).

However, additional effects of mixing different electron populations also contribute to changing the temperature. For example, compared to location 2, the region around location 4-6 has an additional intense population at $v_{||}>0$ smaller than $v_{th,||}$, which leads to a smaller $T_{e||}$. Distributions are often not symmetric between the positive and negative $v_{\perp 1}$ sides relative to the bulk velocity of a few thousand km/s, with more energetic particles extending to the large positive $v_{\perp 1}$ side, e.g., at locations 1, 3 and 4, indicating nongyrotropy of the distribution and partial demagnetization of electrons. The presence of the intense low-energy population can also be more clearly seen in the 2D distributions than in the spectrograms. The parallel electron heating is a typical feature in the reconnection inflow region within the ion diffusion region, whereas the low-energy intense $v_{||}>0$ electrons are probably in the reconnection exhaust moving away from the X-line. The large $T_{e||}$ locations (2 and 3) without much mixture of low-energy intense populations are associated with larger $|B_L|$, i.e., at larger distances from the current layer mid-plane, consistent with the expectation of being closer to the inflow side than locations 5 and 6 with smaller $T_{e||}$ and $|B_L|$. The lower-hybrid wave fluctuation is associated with the corrugation of the current sheet so that the spacecraft alternatively sample the inflow (like locations 2- 3) and outflow (like locations 5-6) sides of the separatrix, leading to variations of the temperature due to different amounts of the mixture between the inflowing and outflowing populations. The corrugation is similar to that observed in fluctuations near the lower-hybrid frequency close to the magnetopause reconnection EDR (Ergun et al., 2017, 2019; Wilder et al., 2019).

Another example for electron temperature modulation on 2017-07-26 is shown in Figure 11 (No. 15), where the corrugation effect is more significant. The correlation coefficient between ϕ and total T_e is 0.46. $T_{e\parallel}$ and $T_{e\perp}$ are anti-correlated. The corrugation effect associated with different amount of mixing of different electron populations can be seen in the $v_\parallel$ spectrogram where low-energy intense populations contribute to the decrease of $T_{e\parallel}$, e.g., around 00:03:49.0 UT, and can be seen in the $v_{\perp 2}$ spectrogram where the loss of particles with $|v_{\perp 2}| > \sim 2 \times 10^4$ km/s contributes to the decrease of $T_{e\perp}$, e.g., 00:03:48.8-00:03:49.0 UT. Five selected 2D distributions are shown on the right. Location 1 has a clear asymmetry between the positive and negative $v_\parallel$ sides, indicating the location to be on the outflow side of the separatrix. The $v_\parallel<0$ part is intense with a low $T_{e\perp}$, which is the inflow population moving towards the X-line. The $v_\parallel>0$ part has a broader distribution along $v_\perp$, which is the outflowing population away from the X-line. Distributions like at locations 2 and 3 have relatively symmetric distributions along $v_\parallel$ for the inflow populations at small $v_\perp$, indicating the locations to be on the inflow side of the separatrix. Comparing distributions 3 and 5, the addition of the hotter outflowing population is consistent with the $T_{e\perp}$ increase. The mixture between the $T_{e||} > T_{e\perp}$ inflow population and the $T_{e||} < T_{e\perp}$ outflowing population leads to the anti-correlation between $T_{e||}$ and $T_{e\perp}$. In addition to the effect of the current sheet corrugation, the wave potential also plays a role in modulating the temperature in this event. The temperature variations are associated with the spectrogram inflation and compression (Figures 11e-11f). For example, the modulation along $v_{||}$ is clear at the velocities near v_{th} from locations 3 to 4; the modulation along $v_{\perp}$ can be seen between locations 4 and 5.

The correlation between ϕ and the total T_e for each event is listed in Table 1. We find that when the correlation coefficient is greater than 0.3, the correlation is clearly visible. There are 6 out of 14 events that have such good correlations. The correlation is a demonstration of acceleration/deceleration by the wave potential as well as the alternating sampling of inflow and outflow sides of the corrugated separatrix region. We examined the simulation data published in Wang et al. (2021a), and found that the ϕ-T_e correlation becomes unclear at the later stage of the wave development (not shown), which is one possible reason why not all the events exhibit clear correlations.

6. Twists of electron flows and magnetic fields

Inside the lower-hybrid wave field, vortices in the background flow frame can form, together with twisting of magnetic field lines. The simulation result (Figure 5 in Wang et al., 2021a) shows that the twist directions of the electron flow ($(\boldsymbol{\nabla} \times \boldsymbol{V_e})_{||} \sim (\boldsymbol{\nabla} \times \boldsymbol{V_{E\times B}})_{||}$) and magnetic fields ($(\nabla \times \boldsymbol{B})_{||} \sim J_{||}$) are not always the same, where the parallel direction is relative to the background **B**. The vortex structures are mostly on the exhaust side of the X-line, where both the DC and fluctuating $J_{||}$ are mainly carried by the electron population with a bulk velocity away from the X-line in the exhaust region. The dominance of the bulk velocity by the outflowing population is related to its larger density than the inflowing population, since overall the density is increased from the inflow to the outflow region. Figure 12a illustrates how $J_{||}$ is modulated in the wave field, for an example region with $B_L>0$. The illustrated situation has a diverging electric field. The left panel has the angle (θ_{kB}) between $\boldsymbol{k}$ and the background magnetic field slightly smaller than 90°, so $E_{||}$ due to the projection of the wave electric field along the magnetic field points towards -L (+L) in the upper (lower) half of the region, as marked by light blue arrows. For typical lower-hybrid drift instabilities, the wave V_{ph} is smaller than the electron drift speed in the ion frame, so electrons around the bulk velocity move towards the $\boldsymbol{k}$ direction relative to the wave field. When electrons move towards the center of the diverging E field region in the upper half, they experience $E_{||}$ towards the -L direction, so electrons away from the X-line (towards +L) are accelerated and those towards the X-line (towards -L) are decelerated, as illustrated by the red arrows. Therefore, the motions of electrons both moving away from and towards the X-line contribute to enhancing $V_{e||}$ around the center of the diverging E field region, and $J_{||}$~$(\nabla \times \boldsymbol{B})_{||}$ (opposite to $V_{e||}$) is enhanced towards the -L direction. Meanwhile, $dB_{||}$ that is proportional to ϕ is positive. $(\boldsymbol{\nabla} \times \boldsymbol{V}_{\boldsymbol{E}\times\boldsymbol{B}})_{||}$ is opposite to $dB_{||}$ since the vortical electron $\boldsymbol{E} \times \boldsymbol{B}$ current induces $dB_{||}$ at the vortex center. Thus, $(\boldsymbol{\nabla} \times \boldsymbol{V}_{\boldsymbol{E}\times\boldsymbol{B}})_{||}$ is enhanced towards the -L direction, same with $(\nabla \times \boldsymbol{B})_{||}$. When θ_{kB} is greater than 90° as illustrated in the right panel, the projected $E_{||}$ has opposite signs at the upper and lower halves of the structure compared to the left panel. The resulting $(\nabla \times \boldsymbol{B})_{||}$ is towards the +L direction, opposite to $(\boldsymbol{\nabla} \times \boldsymbol{V}_{\boldsymbol{E}\times\boldsymbol{B}})_{||}$. Similarly, if in the left panel the magnetic field is reversed to have $B_L<0$ ($\theta_{kB}>90°$), $dB_{||}>0$ in the vortex center would lead to the reversal of $(\boldsymbol{\nabla} \times \boldsymbol{V}_{\boldsymbol{E}\times\boldsymbol{B}})_{||}$, while $(\nabla \times \boldsymbol{B})_{||}$ remains the same, and hence $(\nabla \times \boldsymbol{B})_{||}$ and $(\boldsymbol{\nabla} \times \boldsymbol{V}_{\boldsymbol{E}\times\boldsymbol{B}})_{||}$ are anti-correlated.

Summarizing different situations, we conclude that $(\nabla \times \boldsymbol{B})_{||}$ and $(\boldsymbol{\nabla} \times \boldsymbol{V}_{\boldsymbol{E}\times\boldsymbol{B}})_{||}$ are correlated when θ_{kB}<90° and anti-correlated when θ_{kB}>90°.

With four-spacecraft MMS measurements, we calculate $(\boldsymbol{\nabla} \times \boldsymbol{V}_{\boldsymbol{E}\times\boldsymbol{B}})_{||}$, $(\nabla \times \boldsymbol{B})_{||}$ and $dB_{\parallel}$ at the barycenter, where the parallel direction is along the four-spacecraft average of <1 Hz magnetic field, and the bandpass filtered $\boldsymbol{V}_{\boldsymbol{E}\times\boldsymbol{B}}$ and **B** are used in calculations. Figure 12 shows two examples on 2017-08-10 (No. 7) and 2018-08-27 (No. 10), where the three variables exhibit clear correlating variations.

The 2017-08-10 event exhibits the expected correlation. The presented interval on the 2017-08-10 event is at the +L, B_L>0 side of the X-line, and the angle between $\boldsymbol{k}$ and the background magnetic field is greater than 90° (~108°), so $(\boldsymbol{\nabla} \times \boldsymbol{V}_{\boldsymbol{E}\times\boldsymbol{B}})_{||}$ and $(\nabla \times \boldsymbol{B})_{||}$ are expected to have opposite signs. Figure 12c shows that $(\boldsymbol{\nabla} \times \boldsymbol{V}_{\boldsymbol{E}\times\boldsymbol{B}})_{||}$ and $dB_{\parallel}$ are mostly anti-correlated as expected, indicating that the ‘curl’ calculations are reliable. Figure 12d shows that $(\boldsymbol{\nabla} \times \boldsymbol{V}_{\boldsymbol{E}\times\boldsymbol{B}})_{||}$ and $(\nabla \times \boldsymbol{B})_{||}$ are indeed mostly anti-correlated as expected.

In contrast, the presented interval on 2018-08-27 shows opposite correlations between the two quantities from the expectation. The interval is at the -L, B_L<0 side of the X-line, and the angle between $\boldsymbol{k}$ and the background magnetic field is smaller than 90°, so $(\boldsymbol{\nabla} \times \boldsymbol{V}_{\boldsymbol{E}\times\boldsymbol{B}})_{||}$ and $(\nabla \times \boldsymbol{B})_{||}$ are expected to have the same sign. The anti-correlation between $(\boldsymbol{\nabla} \times \boldsymbol{V}_{\boldsymbol{E}\times\boldsymbol{B}})_{||}$ and $dB_{\parallel}$ (Figure 12f) also indicates the reliability of the calculation. However, $(\boldsymbol{\nabla} \times \boldsymbol{V}_{\boldsymbol{E}\times\boldsymbol{B}})_{||}$ and $(\nabla \times \boldsymbol{B})_{||}$ are mainly anti-correlated (Figure 12g).

Out of the 16 events, 7 events exhibit clear correlations between $(\nabla \times \boldsymbol{V}_{\boldsymbol{E}\times\boldsymbol{B}})_{||}$ and $(\nabla \times \boldsymbol{B})_{||}$, where 5 events have the signs consistent with the expectation. As explained above, the sign expectation between $(\nabla \times \boldsymbol{V}_{\boldsymbol{E}\times\boldsymbol{B}})_{||}$ and $(\nabla \times \boldsymbol{B})_{||}$ is for the region where outflowing electrons dominate and carry the parallel current. In the simulation (Figure 5 in Wang et al. (2021a)), the sign is different from the above expectation around the vortex boundary on the large |N| distance side from the mid-plane, at the main mixing interface between inflow and outflow electrons. For the 2018-08-27 event, the spacecraft transits between the inflow-dominant and outflow-dominant regions around 12:15:42.0 UT (Figure 10). The alternating sampling between the two regions partially contributes to the temperature variation, and may also cause unexpected correlations between $(\nabla \times \boldsymbol{V}_{\boldsymbol{E}\times\boldsymbol{B}})_{||}$ and $(\nabla \times \boldsymbol{B})_{||}$. The distributions shown in Figure 10 confirm such an effect: locations 4-5 near 12:15:42.0 UT have $(\nabla \times \boldsymbol{B})_{||}<0$ corresponding to enhancement of $V_{e||}>0$, and the $V_{e||}$ is contributed by the addition of intense outflowing population at $v_{||}>0$ in the distribution compared to locations 2-3. The simulation (Wang et al., 2021a) also shows that as the vortices develop into the later stage, they become more and more irregular, and correlations of these quantities become less clear, which may be a possible explanation for the events without clear correlations between the two.

7. Discussions about the presence of lower-hybrid waves in the EDR

We find the presence of lower-hybrid waves in all 12 EDR events with wave power enhancements close to f_{lh}, and the wave extends to the current sheet mid-plane. The events have guide field levels from near-zero to ~30%. What is the nature of these waves, and how and where are they generated?

The first possibility is the lower-hybrid drift instability triggered by the local EDR condition. For strong guide field cases, it was demonstrated with the linear instability analysis and a particle-in-cell simulation that the conditions associated with a density gradient in the EDR can be unstable to the lower-hybrid drift instability and generate the short-wavelength mode wave, since the guide field enables the plasma beta to remain low to facilitate the instability (Chen et al., 2020; Ng et al., 2020).

For low guide field cases, e.g., below 10%, we have tested the linear instability analysis for the lower-hybrid drift instability, based on the plasma and field conditions derived from the observation. For an example event of No. 5 on 2017-07-11 (Torbert et al., 2018), the result shows positive growth rates with the maximum at $k\rho_e$=0.60 (not shown), not far from the observed $k\rho_e$=0.41. The instability analysis suggests the peak growth at 1.03 f_{lh}. The observed wave property is derived from signals at a few Hz, higher than f_{lh}~1 Hz, because the short wave observation duration of ~1 s cannot provide reliable information about the wave property at lower frequencies. The limitation in our observation analysis makes it impossible to have more detailed comparisons with the linear instability analysis; however, the instability analysis indicates that the conditions at low guide field EDR can be unstable to the lower-hybrid drift instability. We do not get positive growth rates from the instability analysis for other events with <10% guide field. The failure of getting the instability could be partly due to the uncertainties in deriving EDR plasma and field conditions (especially the pressure gradient) and the fact that the conditions unstable to the instability are already changed after the wave is excited.

The second possibility for the wave presence at a position (e.g., current sheet mid-plane within the EDR) is that the wave is propagated/penetrated from other locations. Figure 13 shows the profile of V_{eL} from a 3D particle-in-cell simulation of reconnection with zero guide field analyzed in Wang et al. (2021a). The fluctuations marked by an oval correspond to short-wavelength mode lower-hybrid waves. By examining the time evolution, the wave is first generated at the separatrix region, and the wave coverage along N expands towards both positive and negative N directions. Close to the X-line (L=3~6 d_i), the wave structure penetrates all the way to the mid-plane. In terms of the L extent, the wave starts at separatrices far from the X-line (>8 d_i), and the closer locations develop the wave later. The entire intense outflow jet up to L~4.5 d_i exhibits clear deviations from the $\boldsymbol{E} \times \boldsymbol{B}$ drift, so we can roughly regard it as the EDR. However, the closest location for the short-wavelength mode wave is at L~3 d_i, where the reconnection exhaust opening angle starts to become larger, forming separatrices with the density gradient much further away from the mid-plane. The same scenario also exists in the simulation of 10% of the guide field (not shown). Such a simulation result provides supporting explanations for the lower-hybrid waves observed in the EDR inside the electron outflow jet, e.g., event No. 10 on 2018-08-27 around 12:15:43 UT. In the event (Figure 1a), the wave exists from the separatrix region with large B_L amplitudes to the mid-plane, while the V_{eL} jet only exists close to the mid-plane (Figure 1c), so the location is analogous to that at L of 3~4.5 in Figure 13. Therefore, it is likely that the wave is generated near the separatrix and penetrates to the mid-plane.

In the zero guide field simulation (Wang et al., 2021a), only the long-wavelength mode wave exists further closer to the mid-plane within ~3 d_i. We note that there may be uncertainties when comparing properties like $k\rho_e$ for the short- and long-wavelength modes. The $k\sqrt{\rho_i\rho_e}\sim 1$ condition for the long-wavelength mode in theoretical and simulation studies (e.g., Daughton, 2003) is based on the temperature at the current sheet mid-plane and the upstream asymptotic magnetic field. In our simulation, the wave at the X-line has $k\sqrt{\rho_i\rho_e}$ =0.8 using the same normalization, but $k\rho_e$ =1.0 if using the parameters at the edge of the EDR, which is also the edge of the wave region. The latter way of normalization is similar to what we do in the observation. A more distinguishing feature for the 'long-wavelength' mode wave at the X-line in the simulation is that the fluctuating electric field is almost entirely supported by the $\nabla \cdot \boldsymbol{P_e}$ term, with little contribution from $-\boldsymbol{V_e} \times \boldsymbol{B}$ (details not shown). In observation events, we see that about 1/4 events have significant $\nabla \cdot \boldsymbol{P_e}$ contribution, which may indicate that the properties of these waves have some similarities with the 'long-wavelength' mode, instead of exactly the short-wavelength mode. On the other hand, the well-established 2017-07-11 event has measurements at L~0, but the lower-hybrid fluctuations in E_N are almost balanced with those in $-\boldsymbol{V_e} \times \boldsymbol{B}$ (not shown). Together with the linear instability analysis, it suggests that the short-wavelength mode wave is excited in the central EDR region (L~0), which is beyond our simulation prediction.

Besides the typical lower-hybrid drift waves, we also find events with the dominant propagation along N (event No. 1, unlike typical properties) and broadband fluctuations with comparable amplitudes in all electric and magnetic field components like part of the turbulence spectra (No. 6). Such cases also lead to fluctuations near the lower-hybrid frequency in the EDR, and future efforts are needed to better understand them.

8. Conclusions and discussions

In this paper, we investigate waves close to the lower-hybrid frequency (loosely defined as lower-hybrid waves) inside and immediately outside the magnetotail reconnection EDR. The wave fluctuations are observed in all the identified EDR with the guide field level from nearly zero to ~30%

For about half of the events, the wave propagation is mainly in the L-M plane, consistent with known lower-hybrid drift waves. However, about half of the events have the wave number direction deviating from the L-M plane by more than 20°, and one event has the propagation almost along N, but the reasons are not yet well understood. Although we do not find a pattern for all events with a significant N component of the wave vector, the case that is presented in section 3.2.2 is special. It has the propagation almost entirely along the current sheet normal, while the normal is mainly along Y_{GSM}, indicating that the propagation of the lower-hybrid wave may couple with the large-scale (ion gyro-radius scale) current sheet corrugation possibly associated with the kink instability and the lower-hybrid wave appears to propagate along the normal direction of the local tilted current sheet.

Regarding the fluctuating magnetic field components, the dominant component is not always along the background magnetic field as in waves at the current sheet boundary layer with strong background magnetic fields far from the reconnection diffusion region, e.g., events 7 and 8 (listed in Table 1). The perpendicular magnetic field fluctuations can be generated due to oblique propagation (e.g., Graham et al., 2019). In addition, field-line twisting in the vortex structures is another way to produce perpendicular magnetic fluctuations, which is explicitly observed in multiple events of this study with the quantity of $(\nabla \times \boldsymbol{B})_{||}$. Event No. 6 has comparable fluctuations in all three components, and the wave power spectrograms have enhanced wave powers in a large frequency range up to ~100 Hz (Figures 7f-7g). It is possible that turbulence is developing in the current sheet (e.g., Ergun et al., 2018), and the wave fluctuations close to the lower-hybrid frequency are part of the turbulence field.

Usually the electron motion is dominated by the $\boldsymbol{E} \times \boldsymbol{B}$ drift in the lower-hybrid wave field. However, we find that about 1/4 of the events have a significant contribution of the $\nabla \cdot \boldsymbol{P}_e$ term for the wave electric field, comparable or greater than the $-\boldsymbol{V_e} \times \boldsymbol{B}$ term. Such significant demagnetization may be a feature for the lower-hybrid waves close to the EDR, possibly related to the ‘long-wavelength’ mode. The greater contribution of $\nabla \cdot \boldsymbol{P}_e$ close to the EDR is also consistent with the simulation result.

Similar to Chen et al. (2020), we find cases where the wave potential and the electron temperature exhibit correlating fluctuations. The temperature fluctuation is contributed by two factors: (1) the wave potential leads to the acceleration/deceleration of electrons, so that distributions are inflated/compressed; (2) crossings at the corrugated layer near the separatrix makes the spacecraft alternatively sample distributions on the inflow and outflow sides of the separatrix. Comparing the temperature components, the event No. 4 (discussed in Chen et al. (2020)) has $T_{e\perp}$ modulation much greater than that in $T_{e||}$, while other events with good correlations like No. 10 shown in Figure 10 have comparable modulation amplitudes in $T_{e||}$ and $T_{e\perp}$. One main difference is that No. 4 is almost along the current sheet mid-plane, while No. 10 is away from the mid-plane near the separatrix. The corrugation effect could also lead to anti-correlation between $T_{e||}$ and $T_{e\perp}$, such as in event No. 15 (Figure 11), since the inflowing electrons tend to have larger $T_{e||}$ and smaller $T_{e\perp}$ than outflowing electrons.

We use the direct calculation of $(\nabla \times \boldsymbol{V}_{E\times B})_{||}$ and $(\nabla \times \mathbf{B})_{||}$ to examine the magnetic field line twisting in the lower-hybrid waves. Understood with the simulation in Wang et al. (2021a), the fluctuating parallel current is mainly carried by the bulk motion of outflowing electrons, which determines the patterns of the correlation (if θ_{kB}<90°) or anti-correlation (if θ_{kB}>90°) between $(\nabla \times \boldsymbol{V}_{E\times B})_{||}$ and $(\nabla \times \mathbf{B})_{||}$. In observations, most of the events with a good correlation between these two quantities have consistent signs with the prediction, but exceptions exist such as in event No. 10, likely due to the alternating sampling of the inflow and outflow regions due to the current sheet corrugation.

The observation of waves close to the lower-hybrid frequency in the weak-guide field EDR encourages further investigations. The zero-guide field simulation suggests that inside the electron outflow jet but at sufficient distances from the X-line where the separatrices are well away from the jet near the mid-plane, short-wavelength mode waves can be excited near the separatrix and penetrates to the mid-plane. The simulation does not show short-wavelength mode wave right around the L location of the X-line as MMS observed, but the linear instability provides hints that the observed EDR condition may be unstable to the wave.

Acknowledgments

The research was supported in part by DOE Grant No. DESC0016278, NSF Grant No. AGS-2010231, NASA 80NSSC18K1369, NASA 80NSSC21K1795 and the NASA MMS mission. The French LPP involvement for the SCM instrument is supported by CNES and CNRS. MMS data are available at https://lasp.colorado.edu/mms/sdc/public/. The simulation data presented in the figures are available online at Wang et al. (2021b). The simulations are performed and archived on Frontera of Texas Advanced Computing Center.

References

Bellan, P. M. (2016), Revised single-spacecraft method for determining wave vector k and resolving space-time ambiguity, J. Geophys. Res. Space Physics, 121, 8589– 8599, doi:10.1002/2016JA022827.

Bowers, K. J., Albright, B. J., Bergen, B., Yin, L., Barker, K. J., & Kerbyson, D. J. (2008). 0.374 pflop/s trillion-particle kinetic modeling of laser plasma interaction on roadrunner. In Proceedings of the 2008 ACM/IEEE Conference on Supercomputing (pp. 63:1–63:11). SC '08. Piscataway, NJ, USA: IEEE Press.

Chen, L.-J., Wang, S., Le Contel, O., Rager, A., Hesse, M., Drake, J., et al. (2020). Lower-hybrid drift waves driving electron nongyrotropic heating and vortical flows in a magnetic reconnection layer. Physical Review Letters, 125. https://doi.org/10.1103/PhysRevLett.125.025103

Cozzani, G., Yu. V. Khotyaintsev, D. B. Graham, M. André, J. Egedal, A. Vaivads, et al. (2021), The structure of a perturbed magnetic reconnection electron diffusion region, https://arxiv.org/pdf/2103.12527.pdf

Daughton,W. (2003). Electromagnetic properties of the lower-hybrid drift instability in a thin current sheet. Physics of Plasmas, 10(8), 3103–3119. https://doi.org/10.1063/1.1594724

Davidson, R. C., Gladd, N. T., Wu, C. S., and Huba, J. D. (1977), "Effects of finite plasma beta on the lower-hybrid-drift instability," Phys. Fluids 20(2), 301–310.

Ergun, R. E., Tucker, S., Westfall, J., Goodrich, K. A., Malaspina, D. M., Summers, D., et al. (2016). The Axial Double Probe and Fields Signal Processing for the MMS Mission. Space Science Reviews, 199, 167–188. https://doi.org/10.1007/s11214-014-0115-x

Ergun, R. E., Chen, L. J., Wilder, F. D., Ahmadi, N., Eriksson, S., Usanova, M. E., et al. (2017). Drift waves, intense parallel electric fields, and turbulence associated with asymmetric magnetic reconnection at the magnetopause. Geophysical Research Letters, 44, 2978–2986. https://doi.org/10.1002/2016GL072493

Ergun, R. E., Goodrich, K. A., Wilder, F. D., Ahmadi, N., Holmes, J. C., Eriksson, S., et al. (2018). Magnetic reconnection, turbulence, and particle acceleration: Observations in the Earth ' s magnetotail. Geophysical Research Letters, 45, 3338 – 3347. https://doi.org/10.1002/2018GL076993

Ergun, R. E., Hoililjoki, S., Ahmadi, N., Schwartz, S. J., Wilder, F. D., Drake, J. F., et al. (2019). Magnetic reconnection in three dimensions: Modeling and analysis of electromagnetic drift waves in the adjacent current sheet. Journal of Geophysical Research: Space Physics, 124, 10085-10103. https://doi.org/10.1029/2019JA027275

Graham, D. B., Khotyaintsev, Y. V., Vaivads, A., and André, M. (2016), Electrostatic solitary waves and electrostatic waves at the magnetopause, J. Geophys. Res. Space Physics, 121, 3069– 3092, doi:10.1002/2015JA021527.

Graham, D. B., Khotyaintsev, Y. V., Norgren, C., Vaivads, A., André, M., Toledo-Redondo, S., & Burch, J. L. (2017). Lower hybrid waves in the ion diffusion region and magnetospheric inflow regions. Journal of Geophysical Research: Space Physics, 122, 517–533. https://doi. org/10.1002/2016JA023572

Graham, D. B., Khotyaintsev, Y. V., Norgren, C., Vaivads, A., André, M., Drake, J. F., et al. (2019). Universality of lower hybrid waves at Earth's magnetopause. Journal of Geophysical Research: Space Physics, 124, 8727– 8760. https://doi.org/10.1029/2019JA027155

Harvey, C. C. (1998), Spatial Gradients and the Volumetric Tensor, in Analysis methods for multi-spacecraft data, International space science institute, 307-322.

Holmes, J. C., Nakamura, R., Schmid, D., Nakamura, T. K. M., Roberts, O., & Vörös, Z. (2021). Wave activity in a dynamically evolving reconnection separatrix. Journal of Geophysical Research: Space Physics, 126, e2020JA028520. https://doi.org/10.1029/2020JA028520

Karimabadi, H., Daughton, W., Pritchett, P. L., & Krauss-Varban, D. (2003). Ion-ion kink instability in the magnetotail: 1. Linear theory. Journal of Geophysical Research, 108(A11), 1400. https://doi.org/10.1029/2003JA010026

Le Contel, O., Leroy, P., Roux, A., Coillot, C., Alison, D., Bouabdellah, A., et al. (2016). The search-coil magnetometer for MMS. Space Science Reviews, 199, 257–282. https://doi.org/10.1007/s11214-014-0096-9

Le Contel, O., Nakamura, R., Breuillard, H., Argall, M. R., Graham, D. B., Fischer, D.,… Jaynes, A. N. (2017). Lower hybrid drift waves and electromagnetic electron space-phase holes associated with dipolarization fronts and field-aligned currents observed by the Magnetospheric Multiscale mission during a substorm. Journal of Geophysical Research: Space Physics, 122, 12,236–12,257. https://doi.org/10.1002/2017JA024550

Lindqvist, P.-A., Olsson, G., Torbert, R. B., King, B., Granoff, M., Rau, D., et al. (2016). The spin-plane double probe electric field instrument for MMS. Space Science Reviews, 199, 137–165. https://doi.org/10.1007/s11214-014-0116-9

Ng, J., Chen, L.-J., Le, A., Stanier, A., Wang, S., & Bessho, N. (2020). Lower-hybrid-drift vortices in the electron-scale magnetic reconnection layer. Geophysical Research Letters, 47, e2020GL090726. https://doi.org/10.1029/2020GL090726

Norgren, C., Vaivads, A., Khotyaintsev, Y. V., & Andre, M. (2012). Lower hybrid drift waves: Space observations. Physical Review Letters, 109(5), 055001. https://doi.org/10.1103/PhysRevLett.109.055001

Pollock, C., Moore, T., Jacques, A., Burch, J., Gliese, U., Saito, Y.,…Zeuch, M. (2016). Fast plasma investigation for magnetospheric multiscale. Space Science Reviews, 199, 331–406. https://doi.org/10.1007/s11214-016-0245-4

Richard, L., Khotyaintsev, Y. V., Graham, D. B., Sitnov, M. I., Le Contel, O., & Lindqvist, P.-A. (2021). Observations of short-period ion-scale current sheet flapping. Journal of Geophysical Research: Space Physics, 126, e2021JA029152. https://doi.org/10.1029/2021JA029152

Robert, P., Dunlop,M. W., Roux, A., & Chanteur, G. (1998). Accuracy of current density determination. ISSI Scientific Reports Series, 1, 395-418.

Russell, C. T., Anderson, B. J., Baumjohann, W., Bromund, K. R., Dearborn, D., Fischer, D.,…Richter, I. (2016). The magnetospheric multiscale magnetometers. Space Science Reviews, 199, 189–256. https://doi.org/10.1007/s11214-014-0057-3

Sergeev, V., Runov, A., Baumjohann, W., Nakamura, R., Zhang, T. L., Volwerk, M., et al. (2003). Current sheet flapping motion and structure observed by Cluster. Geophysical Research Letters, 30, 1327. https://doi.org/10.1029/2002GL016500

Shi, Q. Q., C. Shen, Z. Y. Pu, M. W. Dunlop, Q.-G. Zong, H. Zhang, C. J. Xiao, Z. X. Liu, and A. Balogh (2005), Dimensional analysis of observed structures using multipoint magnetic field measurements: Application to Cluster, Geophys. Res. Lett., 32, L12105, doi:10.1029/2005GL022454.

Tang, B.-B., Li,W. Y., Graham, D. B., Wang, C., Khotyaintsev, Y. V., Le, A., et al. (2020). Lower hybrid waves at the magnetosheath separatrix region. Geophysical Research Letters, 47, e2020GL089880. https://doi.org/10.1029/2020GL089880

Torbert, R., et al. (2014), The fields instrument suite on MMS: Scientific objectives, measurements, and data products, Space Sci. Rev., 199, 105–135, doi:10.1007/s11214-014-0109-8.

Torbert, R. B., Phan, T. D., Hesse, M., Argall, M. R., Shuster, J., Burch, J. L., et al. (2018). Electron-scale dynamics of the diffusion region during symmetric magnetic reconnection in space. Science, 362(6421), 1391–1395. https://doi.org/10.1126/science.aat2998

Wang, S., Chen, L.-J., Bessho, N., Hesse, M., Giles, B. L., & Moore, T. E. (2019). Ion behaviors in the reconnection diffusion region of a corrugated magnetotail current sheet. Geophysical Research Letters, 46. https://doi.org/10.1029/2019GL082226

Wang, S., Chen, L.-J., Ng, J., Bessho, N., and Hesse, M. (2021a), Lower-hybrid drift waves and their interaction with plasmas in a 3D symmetric reconnection simulation with zero guide field, Phys. Plasmas, 28, 072102, https://doi.org/10.1063/5.0054626

Wang, S., Chen, L.-J., Bessho, N., Ng, J., Hesse, M., Graham, D. B., Le Contel, O., Gershman, D., and Giles, B. (2021b), Lower-hybrid wave structures and interactions with electrons observed in magnetotail reconnection diffusion regions: simulation dataset, doi: 10.5281/zenodo.5651243

Wilder, F. D., Ergun, R. E., Hoilijoki, S., Webster, J., Argall, M. R., Ahmadi, N., et al. (2019). A survey of plasma waves appearing near dayside magnetopause electron diffusion region events. Journal of Geophysical Research: Space Physics, 124 . https://doi.org/10.1029/2019JA027060

Wu, C. S., Winske, D., Papadopoulos, K., Zhou, Y. M., Tsai, S. T., & Guo, S. C. (1983). A kinetic cross-field streaming instability. Physics of Fluids, 26, 1259–1267. https://doi.org/10.1063/1.864285

Zhou, M., et al. (2009), Observation of waves near lower hybrid frequency in the reconnection region with thin current sheet, J. Geophys. Res., 114, A02216, doi:10.1029/2008JA013427

Table 1. Lower-hybrid wave event list

No.	[a]Time	B_g	$\frac{\lvert E\rvert}{\lvert B\rvert V_{ph}}$	[b]dominant B comp	[c]significant $\nabla \cdot \boldsymbol{P}_e$	[d]cc ϕ-T_e	[e]$\nabla \times V_{E\times B}$- $\nabla \times$ B
1	20170617/ 202406.0-202409.0	0.04	3	M		MMS4 0.19	exp. -+, obs. --
2	20170619/ 094323.0-094325.5	0.13	8	-		MMS2 0.15	
3	20170703/ 052649.7-052650.4	0.14	12	M		MMS1 0.21	
4	20170703/ 052707.2-052707.8	0.30	8	M		MMS2 0.65	
5	20170711/ 223402.0-223403.0	0.01	9	L, M		MMS1 0.20	
6	20170726/ 000354.0-000402.0	0.33	10	-		MMS4 0.15	exp. +, obs. +
7	20170810/ 121830.0-121838.0	0.25	8	M	Y	MMS3 0.39	exp. -, obs. -
8	20180821/ 110103.3-110104.4	0.25	2	N	y	MMS2 0.43	
9	20180827/ 114122.0-114126.0	0.07	4	L, M	y	MMS2 0.23	
10	20180827/ 121541.3-121542.7	0.06	4	L		MMS1 0.59	exp. +, obs. -
11	20190906/ 043858.6-043859.6	0.09	16	L		MMS3 0.03	exp. +-, obs. +-
12	20200803/ 010643.2-010645.1	0.03	21	L, M	y	MMS2 0.14	
13	20170619/ 094325.7-094327.7		45	L		MMS3 0.44	exp. +, obs. +
14	20170711/ 223401.2-223401.7		7	N		MMS4 0.05	
15	20170726/ 000347.0-000351.8		4	M, N	Y	MMS1 0.46	exp. -, obs. -
16	20180821/ 110100.5-110101.4		12	L		MMS1 0.23	

Table 1. cont.

No.	Frequency	[f]$J \times B$ method result	[g]Wavelet method result
1	2-10Hz	B_L<0,k=0.029×[-0.038,0.013,**-0.999**]km^{-1}, σ_k=0.004×[0.15,0.19,0.01] km^{-1}, $\sigma_{\hat{k}}$=10°, $k\rho_e$=0.25; Good B_L>0, k=0.034×[0.214,-0.189,**0.958**]km^{-1}, σ_k=0.015×[0.19,0.16,0.08] km^{-1}, $\sigma_{\hat{k}}$=11°, $k\rho_e$=0.13; V_{ph}=666~1518km/s. Good	B_L<0, <V_{ph}>=1198 × [-0.004,-0.163,-0.987]km/s; σ_V=615×[0.12,0.26,0.08]; B_L>0, <V_{ph}>=966km/s × [0.124,-0.501,0.856]km/s; σ_V=620×[0.15,0.19,0.15].
2	3-7Hz	k=0.017×[0.649,-0.498,0.575]km^{-1},	

		σ_k=0.012×[0.30,0.37,0.24] km^{-1}, $\sigma_{\hat{k}}$=24°, $k\rho_e$=0.48, V_{ph}=546~3733 km/s.	
3	4-10Hz	k=0.104×[0.622,-0.295,**0.726**]km^{-1}, σ_k=0.003×[0.08,0.25,0.26] km^{-1}, $\sigma_{\hat{k}}$=19°, $k\rho_e$=0.4, V_{ph}=247~829 km/s. Good	
4	3-8Hz	k=0.024×[**-0.982**,-0.174,0.070]km^{-1}, σ_k=0.001×[0.17,0.13,0.22] km^{-1}, $\sigma_{\hat{k}}$=23°, $k\rho_e$=0.19, V_{ph}=1102~1945 km/s.	
5	4-10Hz	k=0.024× [-0.259,-0.700,0.665]km^{-1}, σ_k=0.007×[0.28,0.17,0.26] km^{-1}, $\sigma_{\hat{k}}$=16°, $k\rho_e$=0.41, V_{ph}=979~2225 km/s. Good	$\langle V_{ph}\rangle$=1481 × [0.060,-0.524,0.849] km/s. σ_V=562×[0.34,0.26,0.24].
6	5-8Hz	k=0.024× [**0.663,-0.746**,0.067]km^{-1}, σ_k=0.017×[0.51,0.38,0.51] km^{-1}, $\sigma_{\hat{k}}$=37°, $k\rho_e$=0.24, V_{ph}=512~4639 km/s.	$\langle V_{ph}\rangle$=1908× [0.669,-0.689,0.277]km/s. σ_V=1819×[0.29,0.37,0.42].
7	1-8Hz	k=0.021× [0.139,**-0.897**,0.419]km^{-1}, σ_k=0.018×[0.48,0.36,0.50] km^{-1}, $\sigma_{\hat{k}}$=33°, $k\rho_e$=0.25, V_{ph}=147~4094 km/s.	$\langle V_{ph}\rangle$= 930× [0.257,-0.920,0.296]km/s. σ_V=626×[0.39,0.35,0.70].
8	6-9Hz	k=0.024× [0.278,**-0.953**,-0.123]km^{-1}, σ_k=0.0008×[0.09,0.11,0.35]km^{-1}, $\sigma_{\hat{k}}$=21°, $k\rho_e$=0.60, V_{ph}=1428~1878 km/s.	$\langle V_{ph}\rangle$= 3715× [-0.503,-0.818,0.279]km/s. σ_V=846×[0.37,0.25,0.28].
9	2-6Hz	k=0.011× [**-0.820**,-0.292,0.492]km^{-1}, σ_k=0.007×[0.48,0.47,0.49] km^{-1}, $\sigma_{\hat{k}}$=39°, $k\rho_e$=0.25, V_{ph}=810~3419 km/s.	$\langle V_{ph}\rangle$= 1539× [-0.885,-0.025,0.464]km/s. σ_V=988×[0.38,0.52,0.47].
10	5-11Hz	k=0.017× [-0.344,**-0.853**,-0.393]km^{-1}, σ_k=0.006×[0.16,0.09,0.28] km^{-1}, $\sigma_{\hat{k}}$=14°, $k\rho_e$=0.49, V_{ph}=2033~5685 km/s. Good	$\langle V_{ph}\rangle$= 3413× [-0.318,-0.911,-0.262]km/s. σ_V=1067×[0.25,0.16,0.42].
11	4.5-7Hz	k=0.016× [**0.805**,-0.333,0.491]km^{-1}, σ_k=0.006×[0.25,0.18,0.36] km^{-1}, $\sigma_{\hat{k}}$=21°, $k\rho_e$=0.29, V_{ph}=1636~3235 km/s.	
12	2-6.5Hz	k=0.011× [-0.368, **-0.910**, 0.190]km^{-1}, σ_k=0.004×[0.26,0.49,0.51] km^{-1}, $\sigma_{\hat{k}}$=39°, $k\rho_e$=0.31, V_{ph}=962~2234 km/s.	$\langle V_{ph}\rangle$= 1798× [-0.367, -0.869, 0.336]km/s. σ_V=1198×[0.0.19,0.31,0.45].
13	5-12Hz	k=0.068× [0.555,**-0.823,**-0.118]km^{-1}, σ_k=0.018×[0.15.0.15,0.15] km^{-1}, $\sigma_{\hat{k}}$=11°, $k\rho_e$=0.61, V_{ph}=467~1244km/s. Good	$\langle V_{ph}\rangle$= 753× [0.634,-0.739,-0.226]km/s. σ_V=1198×[0.19,0.31,0.45].
14	5-13Hz		$\langle V_{ph}\rangle$=1366× [-0.510,**-0.860**,-0.010]km/s. σ_V=428×[0.14,0.11,0.25].
15	3-5Hz	k=0.022× [**-0.823**,-0.562,0.068]km^{-1}, σ_k=0.012×[0.55,0.25,0.38] km^{-1}, $\sigma_{\hat{k}}$=40°, $k\rho_e$=0.11, V_{ph}=532~1754km/s.	$\langle V_{ph}\rangle$=1713× [-0.667,-0.718,0.200]km/s. σ_V=999×[0.20,0.23,0.40].
16	5-7Hz	k=0.026× [-0.140,**-0.968**,-0.206]km^{-1}, σ_k=0.003×[0.25,0.11,0.57]km^{-1},	

		$\sigma_{\hat{k}}$=51°,$k\rho_e$=0.46, V_{ph}=1094~1498 km/s.	

[a]The time interval is used for the wave propagation analysis. The last four events belong to the same current sheets as one of the top ones, while they are additional wave packets away from the mid-plane. [b]The dominant magnetic field fluctuation component is judged by the FFT spectrogram. Events that list two components mean that they have comparable amplitudes; events with '-' means that all three components have comparable amplitudes. [c]A significant contribution is from the $\nabla \cdot \boldsymbol{P}_e$ term for the fluctuating E_N judged by the four-spacecraft force balance terms ('Y') or by deviations between $\mathbf{E}$ and $-\boldsymbol{V}_{\boldsymbol{e}} \times \boldsymbol{B}$ at single spacecraft measurements. [d]The correlation coefficient between the potential of the filtered electric field and the electron temperature at the spacecraft with the highest coefficient is listed. Events with a coefficient higher than 0.3 have visible correlations. [e]Expected (exp.) and observed (obs.) correlation between the parallel component of $\nabla \times \boldsymbol{V}_{E\times B}$ and $\nabla \times \mathbf{B}$. Events without a clear correlation between the two are left blank. [f]ρ_e is the minimum value during the analysis interval, and V_{ph} is obtained from the frequency and $|\mathbf{k}|$ in the frequency range. The standard deviation of the $|\mathbf{k}|$ amplitude and each component of the $\mathbf{k}$ unit vector over frequencies is evaluated as σ_k, and the $\sigma_{\hat{k}}$ represents the standard deviation of angle between each pair $\mathbf{k}$ directions. When the uncertainties of all $\mathbf{k}$ components are smaller than 0.3 and $\sigma_{\hat{k}}$ is smaller than 20°, the result is considered as very reliable (marked as 'Good'). [g]The wave propagation from the wavelet method. <V_{ph}> represents the average result over time and frequencies, and σ_V represents the standard deviation of V_{ph} amplitude and direction. If the method does not give a consistent result over frequencies or times, or the method is not applicable, it is left blank.

Figure Captions

Figure 1. Overview of the electron current layer on 2018-08-27 around 12:15:43 UT with MMS1 measurements (event No. 10). (a) magnetic field. (b) electric field. (c) electron bulk velocity. (d) ion bulk velocity. (e) L and M components of $V_{\perp}$ comparison between $V_{E\times B}$ and V_e. (f)-(g) wavelet power spectrograms of the electric and magnetic fields overplotted with f_{lh}, $f_{ce}/2$, and f_{ce}. (h) The V_{eL} profile from a simulation, where the black arrow illustrates the MMS trajectory during the lower-hybrid wave interval around 12:15:42 UT.

Figure 2. The wave property analysis of the event on 2018-08-27 during 12:15:41.3-12:15:42.7 UT. (a) FFT wave power spectra for the electric field in dashed curves in unit of $(mV/m)^2/Hz$ and the magnetic field in solid curves in unit of nT^2/Hz. The magenta curve is $|\boldsymbol{E}|/(|\boldsymbol{B}|V_{ph})$. The two vertical dashed lines are the average and maximum f_{lh} during the interval. (b) B_L at four spacecraft. (c)-(f) the L, M and N components of the wave propagation direction and the amplitude of V_{ph} obtained from the wavelet phase correlation analysis of B_L. Each curve represents a frequency band in the 5-11 Hz range. (g)-(h) The wave number obtained from the $\boldsymbol{J}\times\boldsymbol{B}$ method. The magnetic field wave power spectrum (black) and the amplitude of **k** (red) are shown in (g), and the components of the **k** unit vector are shown in (h).

Figure 3. Overview of the event on 2018-08-21 (event No. 8). The format is the same as in Figure 1.

Figure 4. The wave property analysis of the 2018-08-21 event during 11:01:03.3-11:01:04.4 UT, between the vertical dashed lines marked in (b)-(g). The format is mostly

the same with Figure 2, except that B_L and B_N from four spacecraft are shown in (b)-(c), and the wavelet phase correlation analysis result in (d)-(g) is performed for B_N.

Figure 5. Overview of the event on 2017-06-17 (event No. 1). The format is the same as in Figure 1.

Figure 6. The wave property analysis of the 2017-06-17 event during 20:04:06-20:04:09 UT. The format is similar to Figure 4. The wavelet phase correlation analysis is performed for B_M. The $\boldsymbol{J} \times \boldsymbol{B}$ analysis is performed for B_L<0 (h-i) and B_L>0 (j-k) parts separately.

Figure 7. Overview of the event on 2017-07-26 (event No. 6). The format is the same as in Figure 1.

Figure 8. The wave property analysis of the 2017-07-26 event during 00:03:54-00:04:02 UT. The format is the same as in Figure 4.

Figure 9. The contribution of $-\boldsymbol{V_e} \times \boldsymbol{B}$ and the $\nabla \cdot \boldsymbol{P_e}$ term to the DC and fluctuating components of E_N, for the 2018-08-27 event No. 10 around 12:15:43 UT (left) and 2017-08-10 event No. 7 (right). (a), (f) B_L at and average over four spacecraft. (b) E_N and $(-\boldsymbol{V_e} \times \boldsymbol{B})_N$ at MMS1. (c)-(e), (h)-(k) E_N and $(-\boldsymbol{V_e} \times \boldsymbol{B})_N$ after subtracting the 1-s sliding average values to represent the fluctuations, at individual spacecraft. (g) Terms in the N component of the electron momentum equation calculated at the spacecraft barycenter. **E** (black) well agrees with the sum (green) of $-\boldsymbol{V_e} \times \boldsymbol{B}$ (blue) and the $\nabla \cdot \boldsymbol{P_e}$ term (red).

Figure 10. Electron heating in the lower-hybrid wave field for the event on 2018-08-27 around 12:15:43 UT (event No. 10), with MMS1 measurements. (a) magnetic field. The 2-8 Hz $dB_{||}$ (red in panel b), electric potential of 2-8 Hz electric fields (c), and the

electron temperature (d) exhibit correlating fluctuations. (e)-(f) reduced 1D spectrograms along $v_{\parallel}$ and $v_{\perp 2}$, where $v_{\perp 2}$ is along the local $\boldsymbol{B} \times (\boldsymbol{E} \times \boldsymbol{B})$ direction. The overplotted black curves mark the electron thermal speed. Vertical dashed lines mark the times for 2D electron distributions in the $v_{\parallel} - v_{\perp 1}$ (g) and $v_{\perp 1} - v_{\perp 2}$ (h) planes, where $v_{\perp 1}$ is along the local $\boldsymbol{E} \times \boldsymbol{B}$ direction. The distributions show the inflation along with the temperature increase and nongyrotropic features.

Figure 11. Electron heating in the event on 2017-07-26 around 00:04:48 UT (event No. 15). The format is the same with Figure 10. The parallel and perpendicular components of T_e exhibit anti-correlations.

Figure 12. Twist of flow and magnetic field lines in the event of 2017-08-10 (event No. 7, left) and 2018-08-27 around 12:15:43 UT (right, event No. 10). (a) Illustration of the $(\nabla \times \boldsymbol{V}_{E\times B})_{||}$ and $(\nabla \times \boldsymbol{B})_{||}$ correlation associated with the electron field-aligned acceleration or deceleration for the bulk population moving along **k** relative to the wave field. The region with diverging electric fields is illustrated, and the left and right panels correspond to $\theta_{kB} < 90°$ and $\theta_{kB} > 90°$, respectively. (b), (e) the magnetic field averaged over four spacecraft. (c), (f) $(\nabla \times \boldsymbol{V}_{E\times B})_{||}$ (black) anti-correlated with $dB_{\parallel}$ (red), consistent with the electron $\boldsymbol{E} \times \boldsymbol{B}$ current inducing $dB_{\parallel}$. (d), (g) $(\nabla \times \boldsymbol{V}_{E\times B})_{||}$ (black) and $(\nabla \times \boldsymbol{B})_{||}$ (blue).

Figure 13. V_{eL} profile from a 3D particle-in-cell simulation of reconnection with zero guide field, cut at an M location. L=0 is at the X-line. The electron outflow jet extends to L~4.5 d_i. The short-wavelength mode lower-hybrid wave (oscillations marked by the oval) develops near the separatrix and penetrates to the mid-plane. The wave exists at L

locations as close to ~3 d_i inside the range of the electron outflow, where the reconnection exhaust opening angle starts to be large and separatrices are well away from the mid-plane. No short-wavelength mode wave exists further closer to the X-line.

Figure 1.

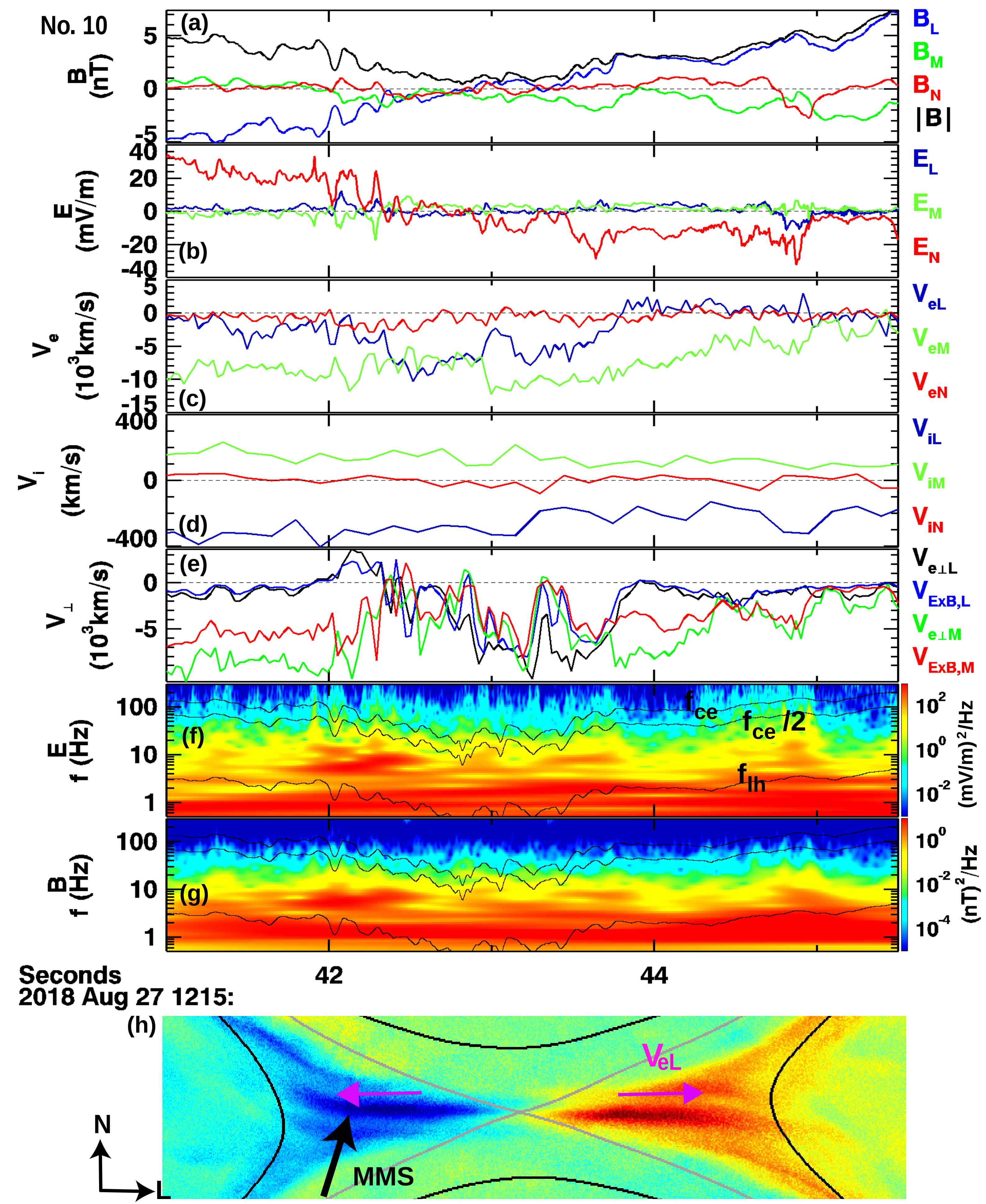

No. 10
(a)
(b)
(c)
(d)
(e)
(f)
(g)
(h)
B (nT)
E (mV/m)
Ve (10^3km/s)
Vi (km/s)
V⊥ (10^3km/s)
E f (Hz)
B f (Hz)
B_L
B_M
B_N
|B|
E_L
E_M
E_N
V_eL
V_eM
V_eN
V_iL
V_iM
V_iN
V_e⊥L
V_ExB,L
V_e⊥M
V_ExB,M
f_ce
f_ce /2
f_lh
(mV/m)^2/Hz
(nT)^2/Hz
Seconds
2018 Aug 27 1215:
42
44
V_eL
MMS
N
L

Figure 2.

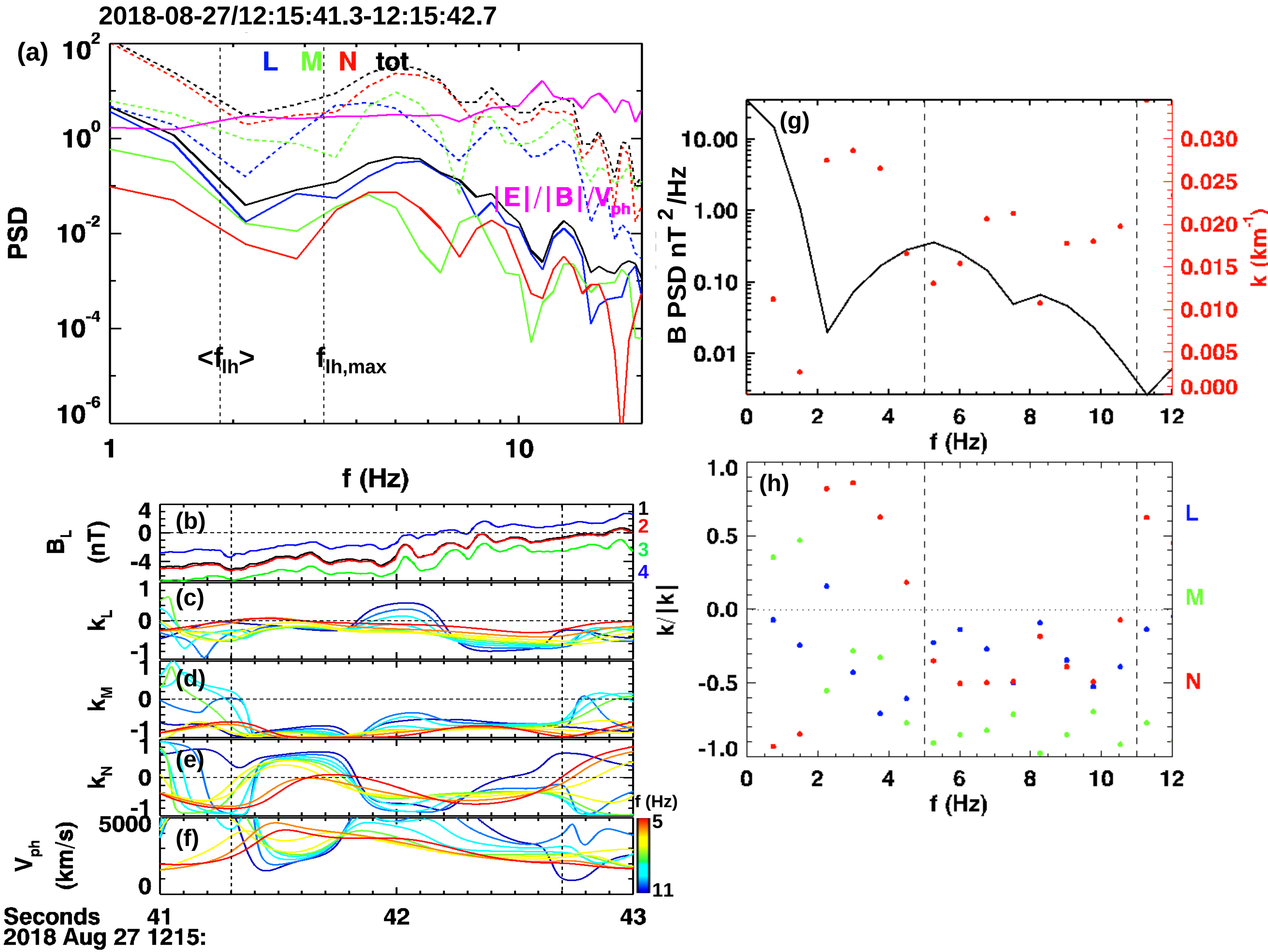

2018-08-27/12:15:41.3-12:15:42.7
(a)
L M N tot
|E|/|B|/V_ph
PSD
<f_lh>
f_lh,max
f (Hz)
(b)
B_L (nT)
1
2
3
4
(c)
k_L
(d)
k_M
(e)
k_N
(f)
V_ph (km/s)
f (Hz)
Seconds
2018 Aug 27 1215:
(g)
B PSD nT^2/Hz
k (km^-1)
f (Hz)
(h)
k/|k|
L
M
N
f (Hz)

Figure 3.

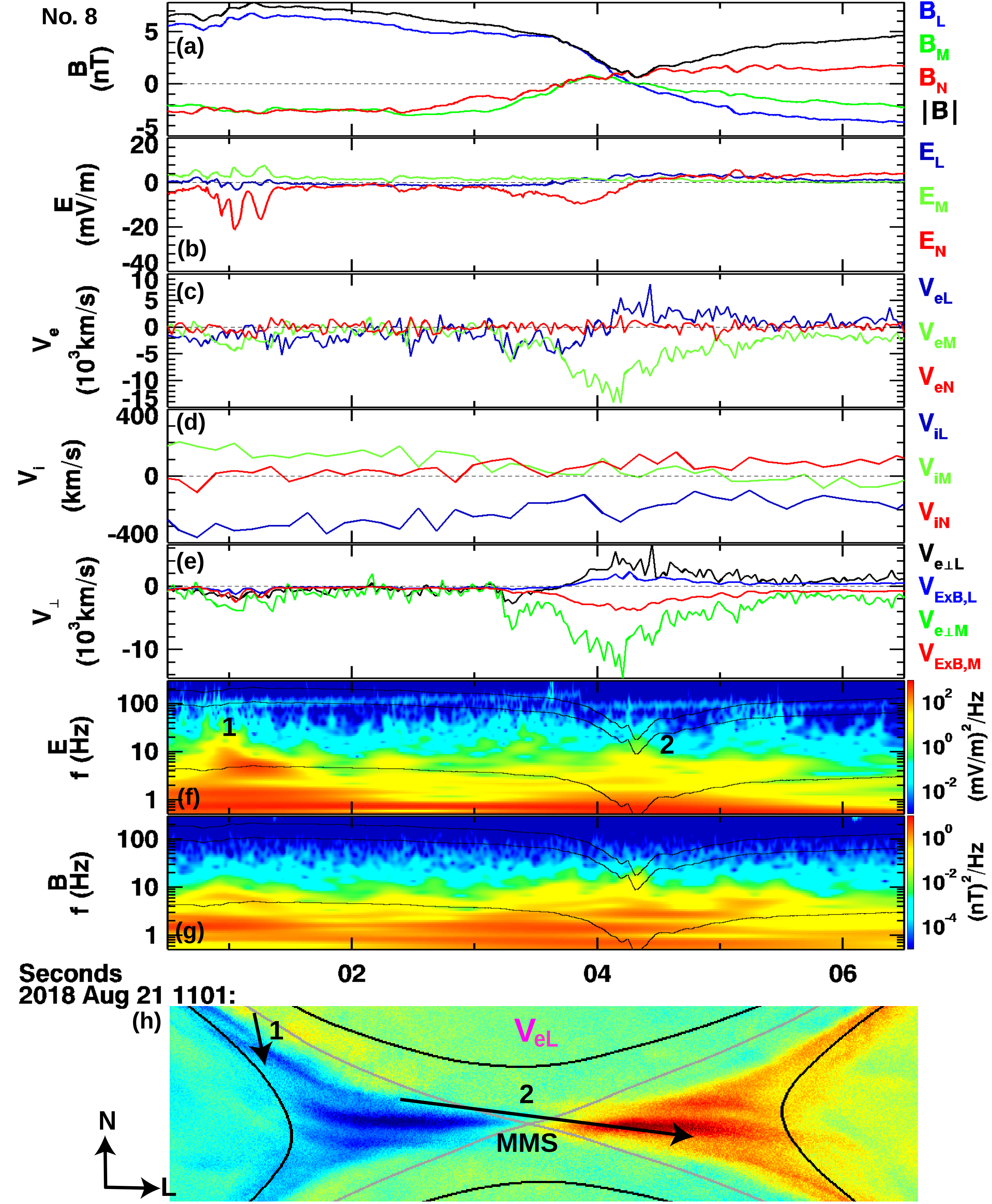
No. 8
B (nT)
(a)
B_L
B_M
B_N
|B|
E (mV/m)
(b)
E_L
E_M
E_N
V_e (10^3km/s)
(c)
V_{eL}
V_{eM}
V_{eN}
V_i (km/s)
(d)
V_{iL}
V_{iM}
V_{iN}
$V_\perp$ (10^3km/s)
(e)
$V_{e\perp L}$
$V_{ExB,L}$
$V_{e\perp M}$
$V_{ExB,M}$
E f (Hz)
(f)
1
2
$(mV/m)^2/Hz$
B f (Hz)
(g)
$(nT)^2/Hz$
Seconds
2018 Aug 21 1101:
02
04
06
(h)
V_{eL}
1
2
MMS
N
L

Figure 4.

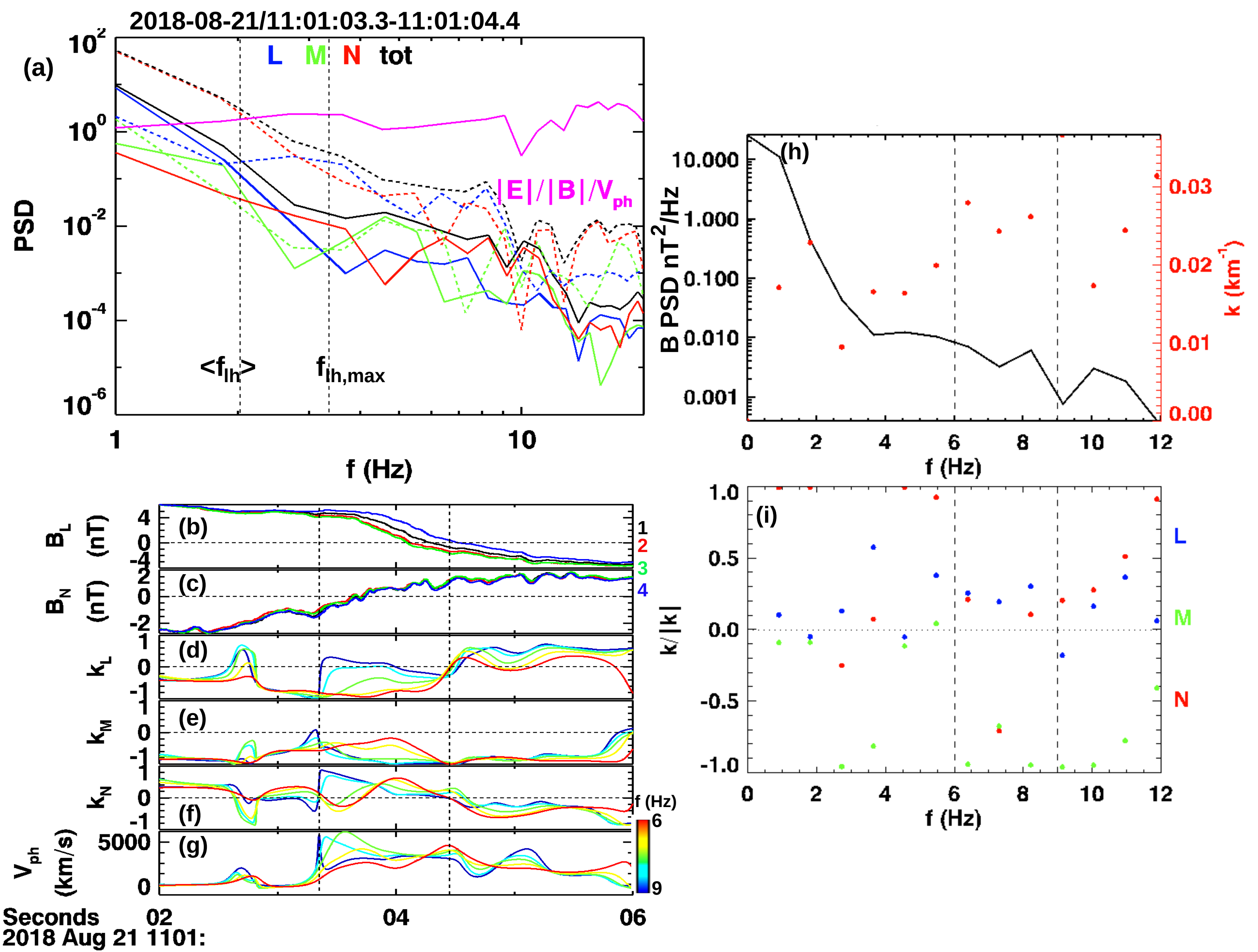

2018-08-21/11:01:03.3-11:01:04.4
(a)
L M N tot
|E|/|B|/V_ph
PSD
<f_lh>
f_lh,max
f (Hz)
(b)
(c)
(d)
(e)
(f)
(g)
B_L (nT)
B_N (nT)
k_L
k_M
k_N
V_ph (km/s)
1
2
3
4
f (Hz)
Seconds
2018 Aug 21 1101:
(h)
B PSD nT^2/Hz
k (km^-1)
f (Hz)
(i)
k/|k|
L
M
N
f (Hz)

Figure 5.

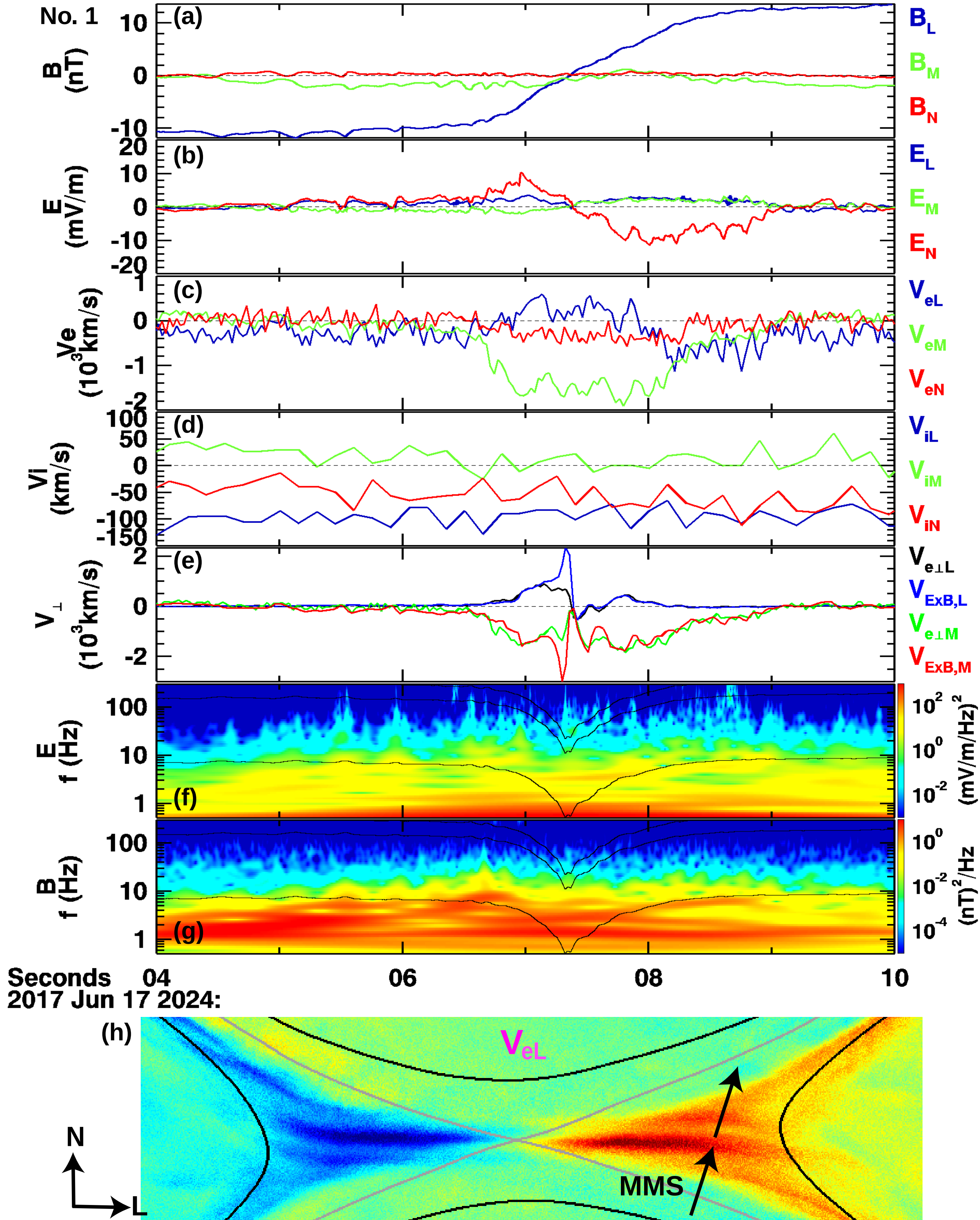

No. 1
(a)
B (nT)
B_L
B_M
B_N
(b)
E (mV/m)
E_L
E_M
E_N
(c)
Ve (10^3km/s)
V_{eL}
V_{eM}
V_{eN}
(d)
Vi (km/s)
V_{iL}
V_{iM}
V_{iN}
(e)
$V_\perp$ (10^3km/s)
$V_{e\perp L}$
$V_{ExB,L}$
$V_{e\perp M}$
$V_{ExB,M}$
(f)
E f (Hz)
(mV/m/Hz)^2
(g)
B f (Hz)
(nT)^2/Hz
Seconds
2017 Jun 17 2024:
04
06
08
10
(h)
V_{eL}
N
L
MMS

Figure 6.

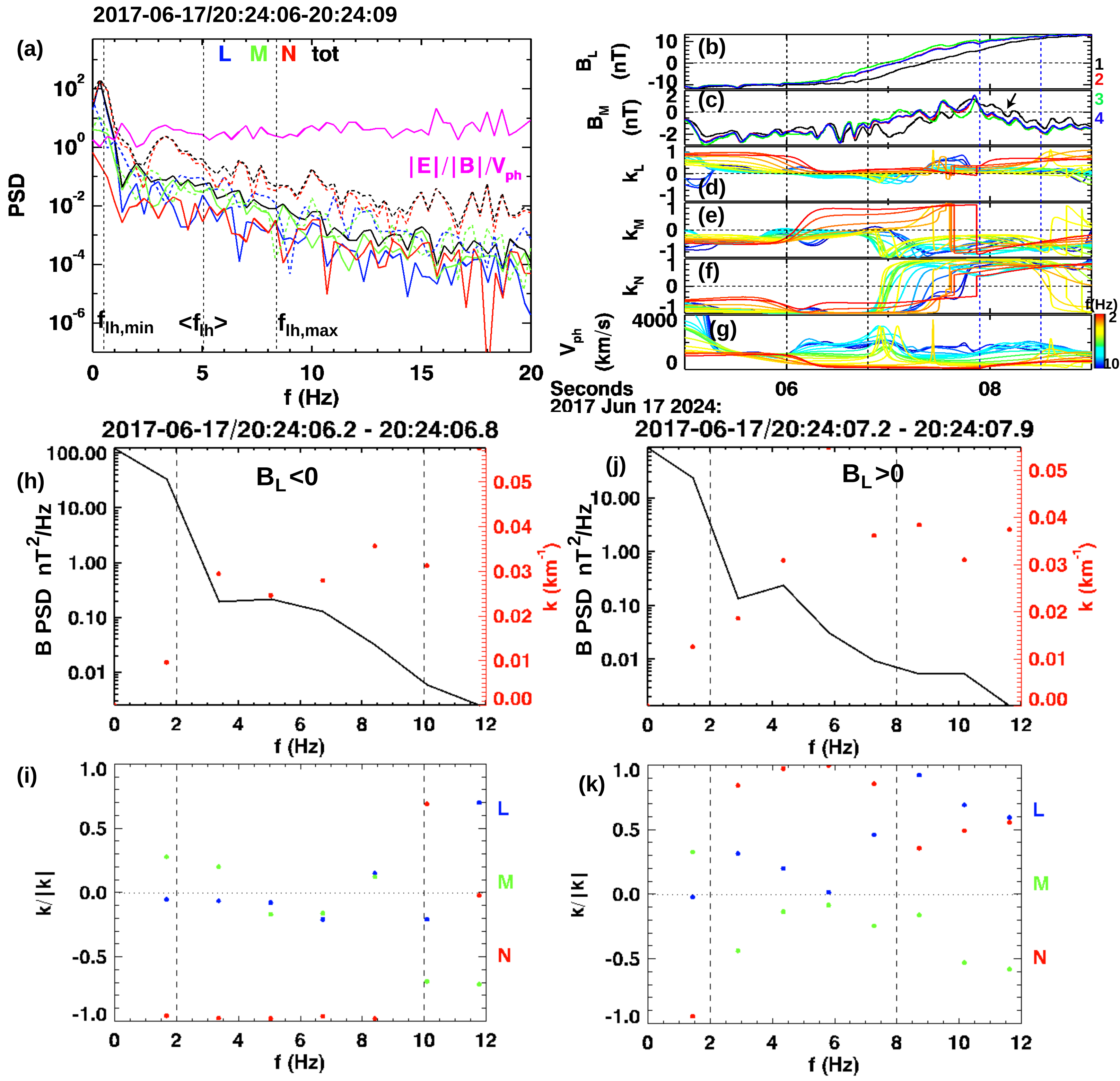

2017-06-17/20:24:06-20:24:09
(a)
L M N tot
|E|/|B|/V_ph
PSD
f_lh,min
<f_lh>
f_lh,max
f (Hz)
(b)
(c)
(d)
(e)
(f)
(g)
B_L (nT)
B_M (nT)
k_L
k_M
k_N
V_ph (km/s)
f(Hz)
Seconds
2017 Jun 17 2024:
2017-06-17/20:24:06.2 - 20:24:06.8
(h)
B_L<0
B PSD nT^2/Hz
k (km^-1)
(i)
k/|k|
2017-06-17/20:24:07.2 - 20:24:07.9
(j)
B_L>0
(k)

Figure 7.

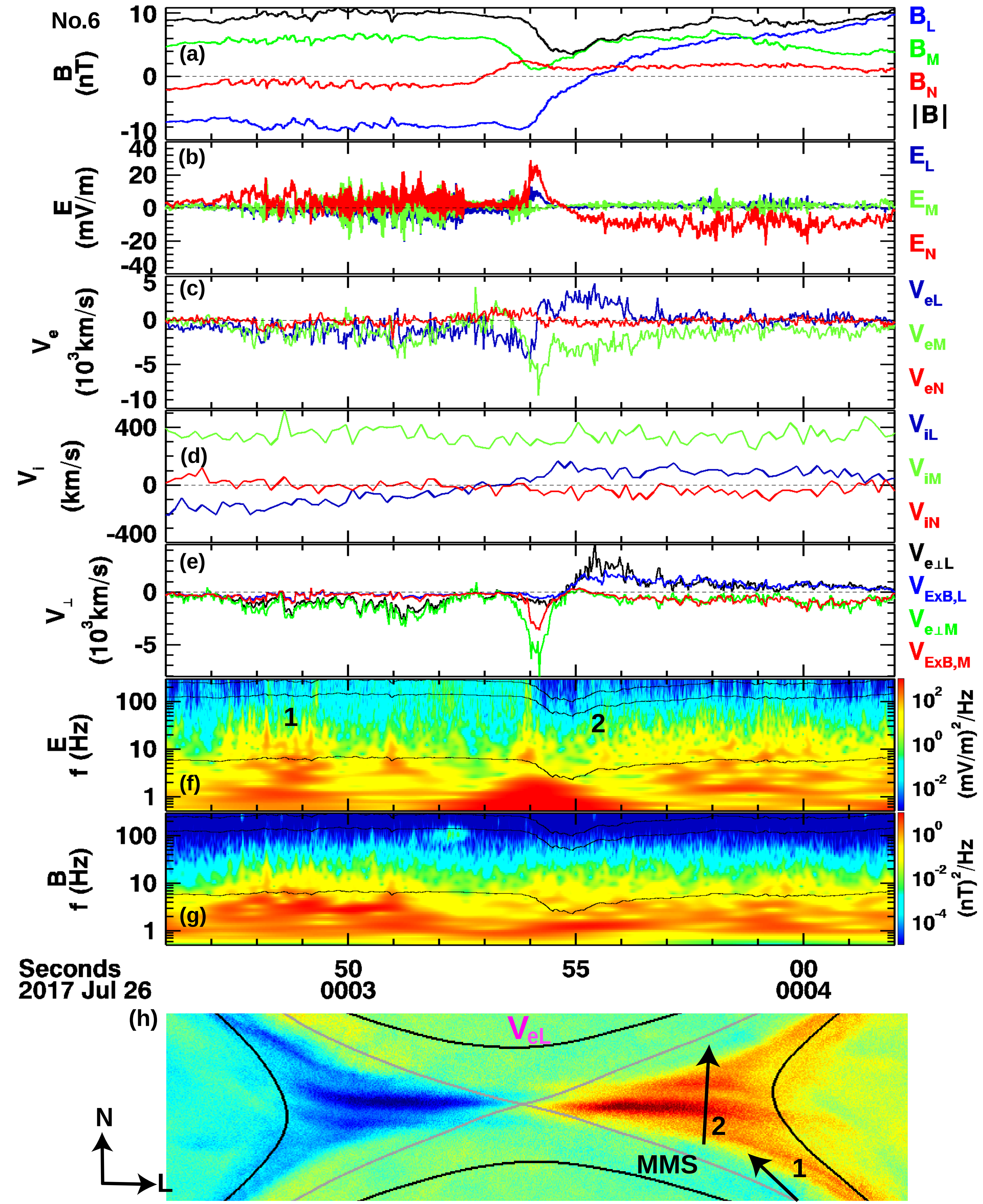

No.6
B (nT)
(a)
B_L
B_M
B_N
|B|
E (mV/m)
(b)
E_L
E_M
E_N
V_e (10^3 km/s)
(c)
V_eL
V_eM
V_eN
V_i (km/s)
(d)
V_iL
V_iM
V_iN
V_⊥ (10^3 km/s)
(e)
V_e⊥L
V_ExB,L
V_e⊥M
V_ExB,M
E f (Hz)
(f)
1
2
(mV/m)^2/Hz
B f (Hz)
(g)
(nT)^2/Hz
Seconds
2017 Jul 26
50
0003
55
00
0004
(h)
V_eL
N
L
MMS
1
2

Figure 8.

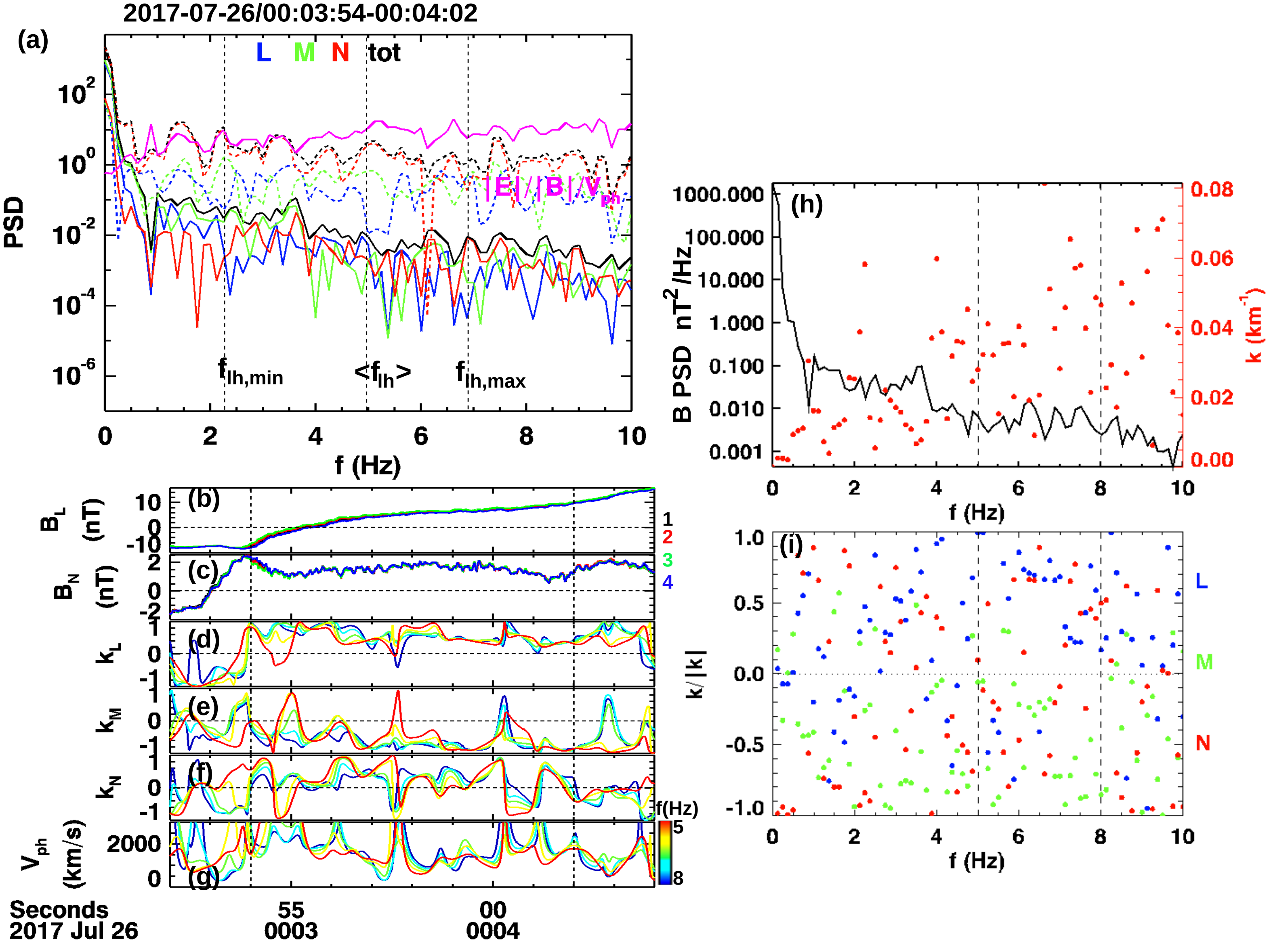

2017-07-26/00:03:54-00:04:02
(a)
L M N tot
|E|/|B|/V_ph
PSD
f_lh,min
<f_lh>
f_lh,max
f (Hz)
(b)
(c)
(d)
(e)
(f)
(g)
B_L (nT)
B_N (nT)
k_L
k_M
k_N
V_ph (km/s)
1
2
3
4
f(Hz)
Seconds
2017 Jul 26
55
0003
00
0004
(h)
B PSD nT^2/Hz
k (km^-1)
(i)
k/|k|
L
M
N

Figure 9.

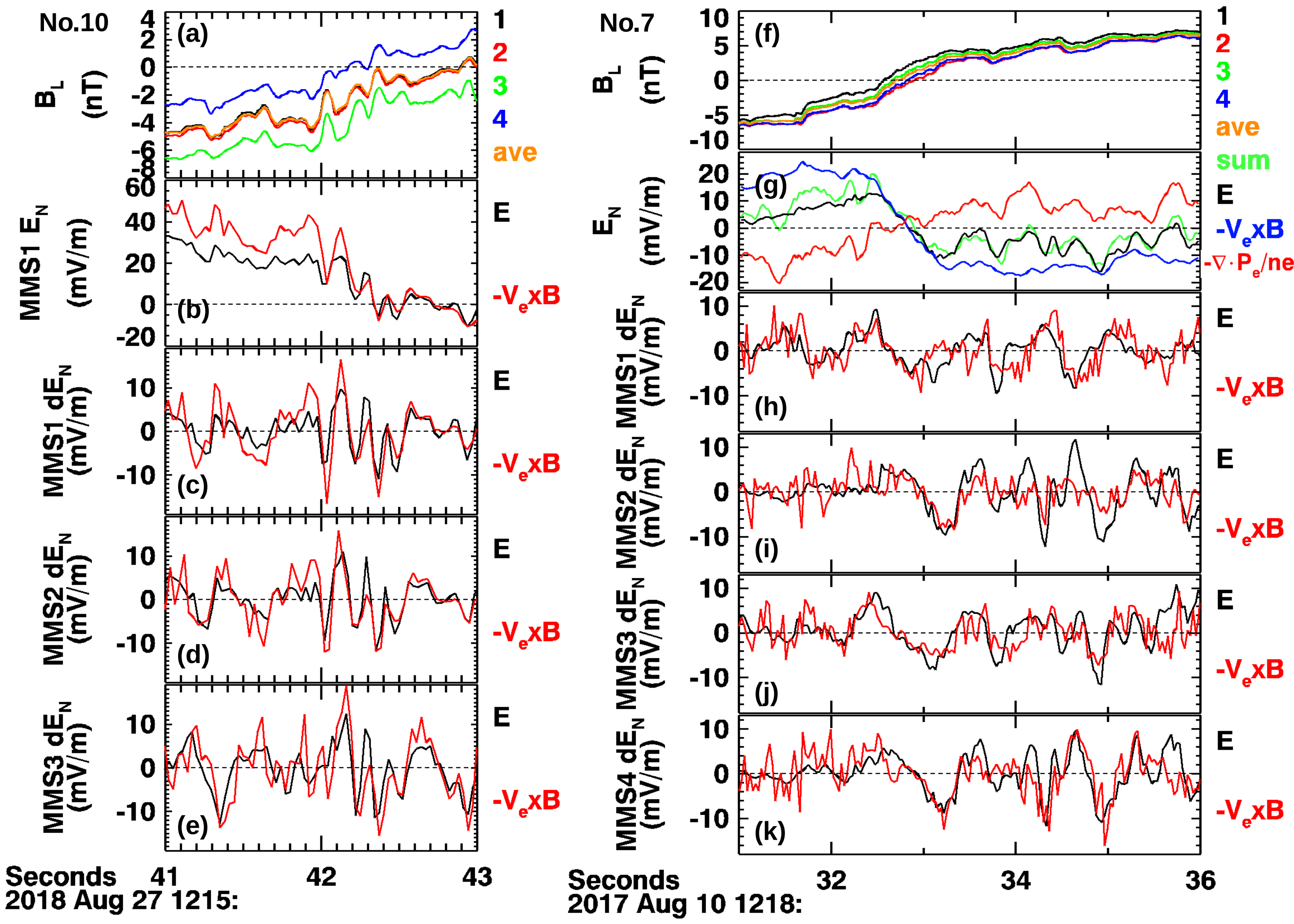

No.10
No.7
(a)
(b)
(c)
(d)
(e)
(f)
(g)
(h)
(i)
(j)
(k)
B_L (nT)
MMS1 E_N (mV/m)
MMS1 dE_N (mV/m)
MMS2 dE_N (mV/m)
MMS3 dE_N (mV/m)
MMS4 dE_N (mV/m)
E_N (mV/m)
1
2
3
4
ave
sum
E
-V_exB
-∇·P_e/ne
Seconds
2018 Aug 27 1215:
2017 Aug 10 1218:

Figure 10.

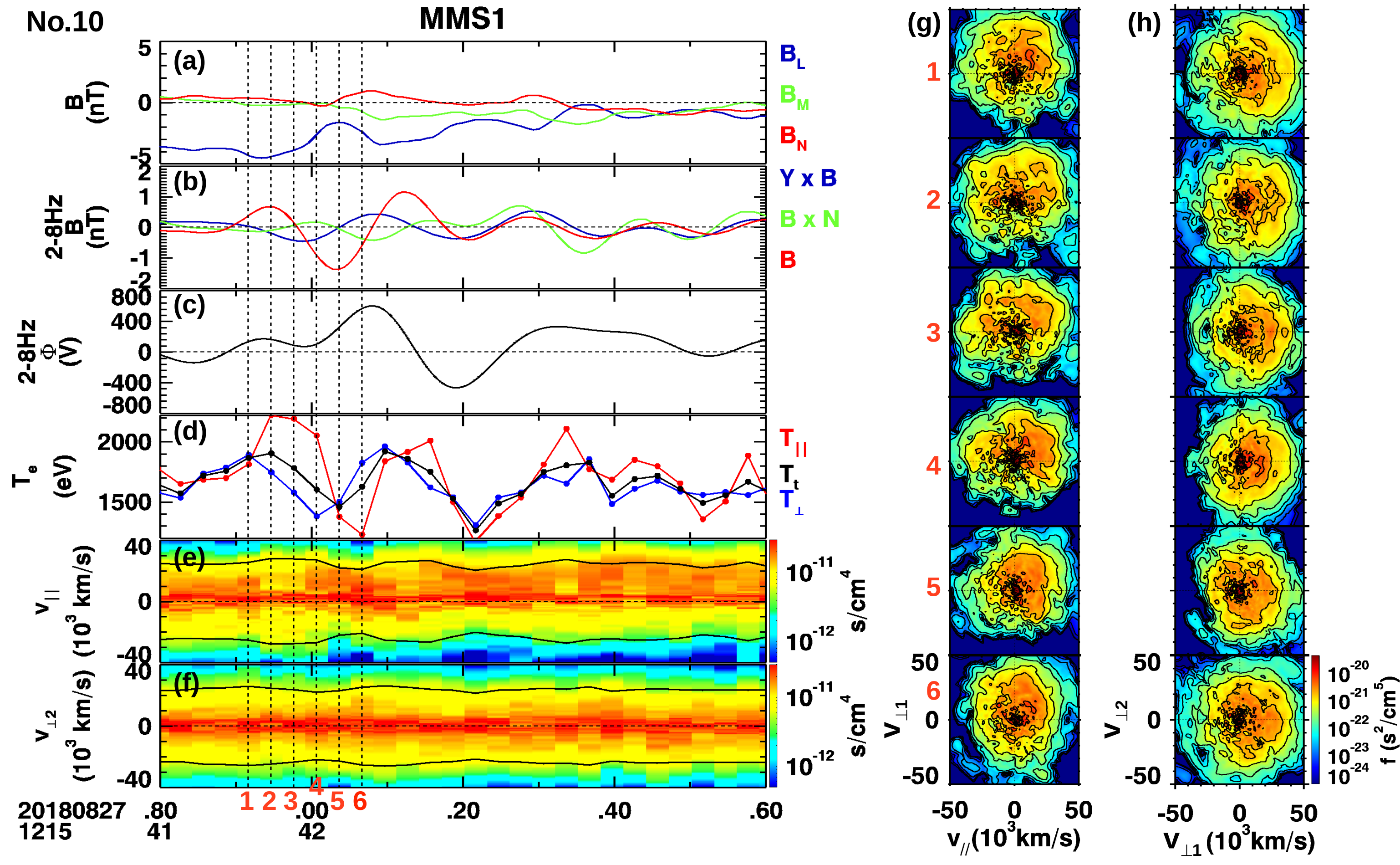

No.10
MMS1
(a)
B (nT)
B_L
B_M
B_N
(b)
2-8Hz B (nT)
Y x B
B x N
B
(c)
2-8Hz Φ (V)
(d)
T_e (eV)
$T_{||}$
T_t
$T_\perp$
(e)
$v_{||}$ (10^3 km/s)
s/cm^4
(f)
$v_{\perp 2}$ (10^3 km/s)
s/cm^4
20180827 1215
.80 41
.00 42
.20
.40
.60
1 2 3 4 5 6
(g)
(h)
$V_{\perp 1}$
$V_{\perp 2}$
$v_{//}$(10^3km/s)
$V_{\perp 1}$ (10^3km/s)
f (s^2/cm^5)

Figure 11.

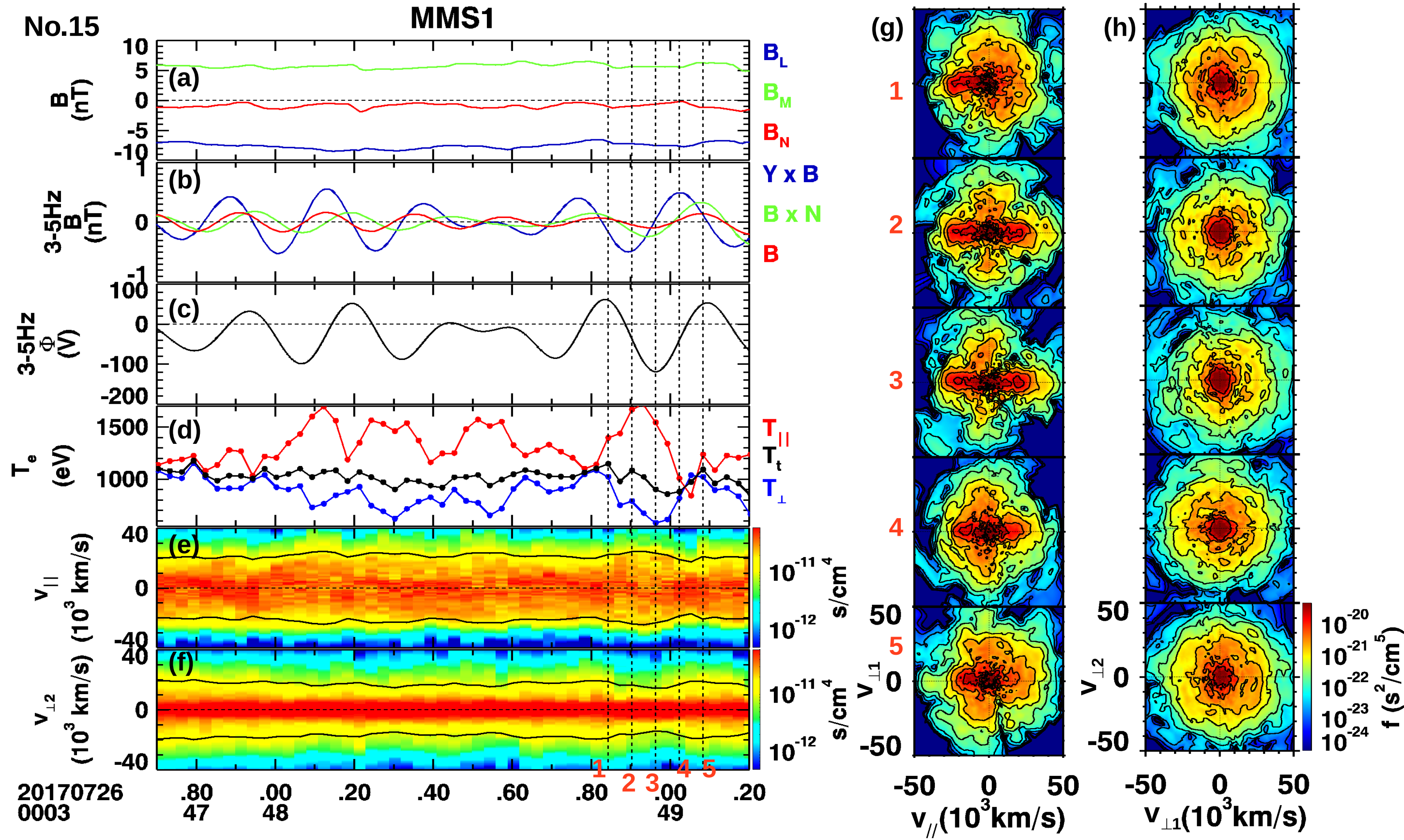

No.15
MMS1
(a)
(b)
(c)
(d)
(e)
(f)
(g)
(h)
B (nT)
3-5Hz B (nT)
3-5Hz Φ (V)
T_e (eV)
$v_{||}$ (10^3 km/s)
$v_{\perp 2}$ (10^3 km/s)
B_L
B_M
B_N
Y x B
B x N
B
$T_{||}$
T_t
$T_\perp$
s/cm^4
f (s^2/cm^5)
$v_{\perp 1}$
$v_{\perp 2}$
$v_{//}$(10^3km/s)
$v_{\perp 1}$(10^3km/s)
20170726
0003
.80 47
.00 48
.20
.40
.60
.80
.00 49
.20
1
2
3
4
5

Figure 12.

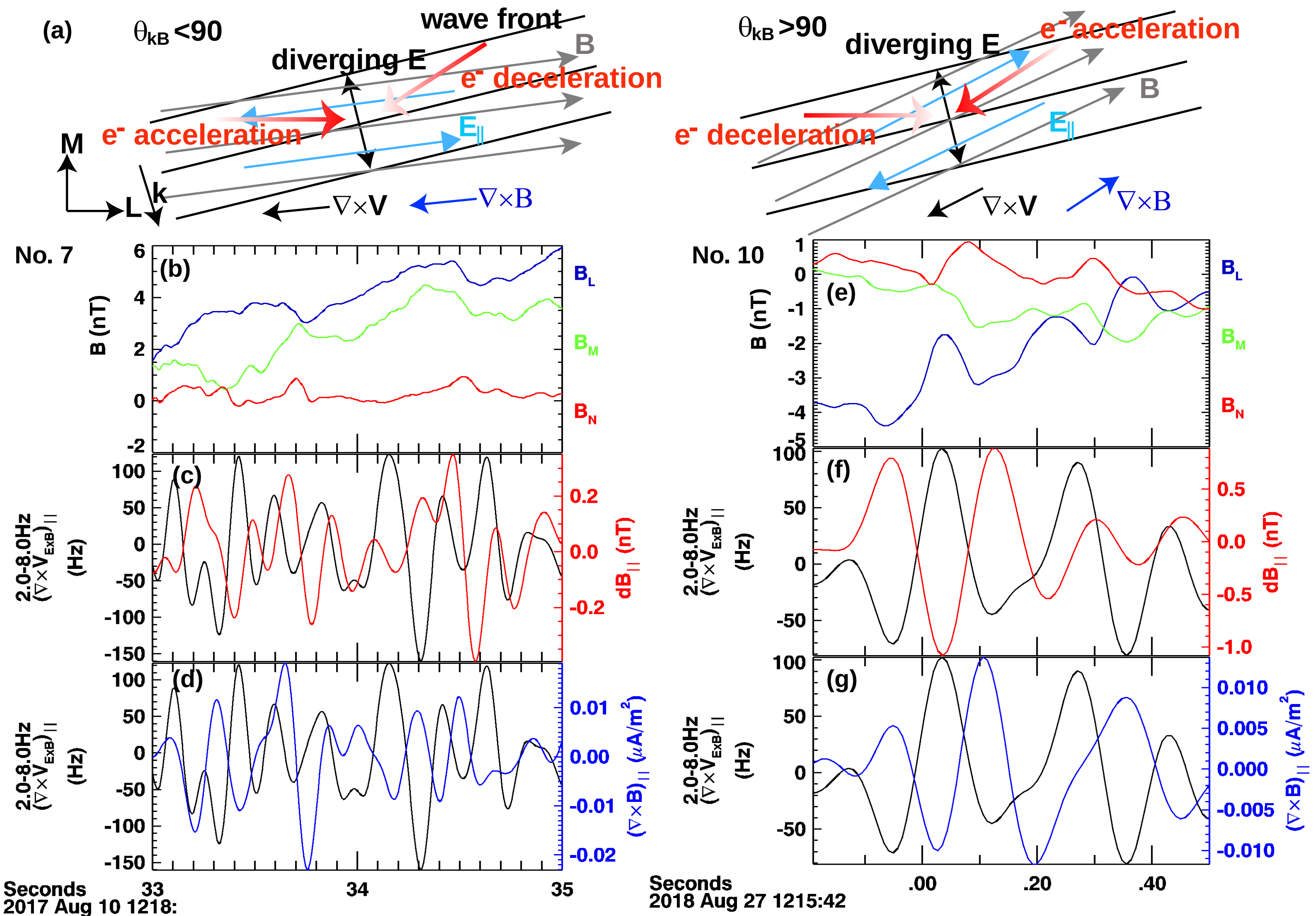

(a)
θkB <90
wave front
diverging E
B
e- deceleration
e- acceleration
E∥
M
L
k
∇×V
∇×B
θkB >90
diverging E
e- acceleration
B
e- deceleration
E∥
∇×V
∇×B
No. 7
(b)
B (nT)
BL
BM
BN
(c)
2.0-8.0Hz (∇×VExB)∥ (Hz)
dB∥ (nT)
(d)
(∇×B)∥ (μA/m2)
Seconds
2017 Aug 10 1218:
33
34
35
No. 10
(e)
(f)
(g)
Seconds
2018 Aug 27 1215:42
.00
.20
.40

Figure 13.

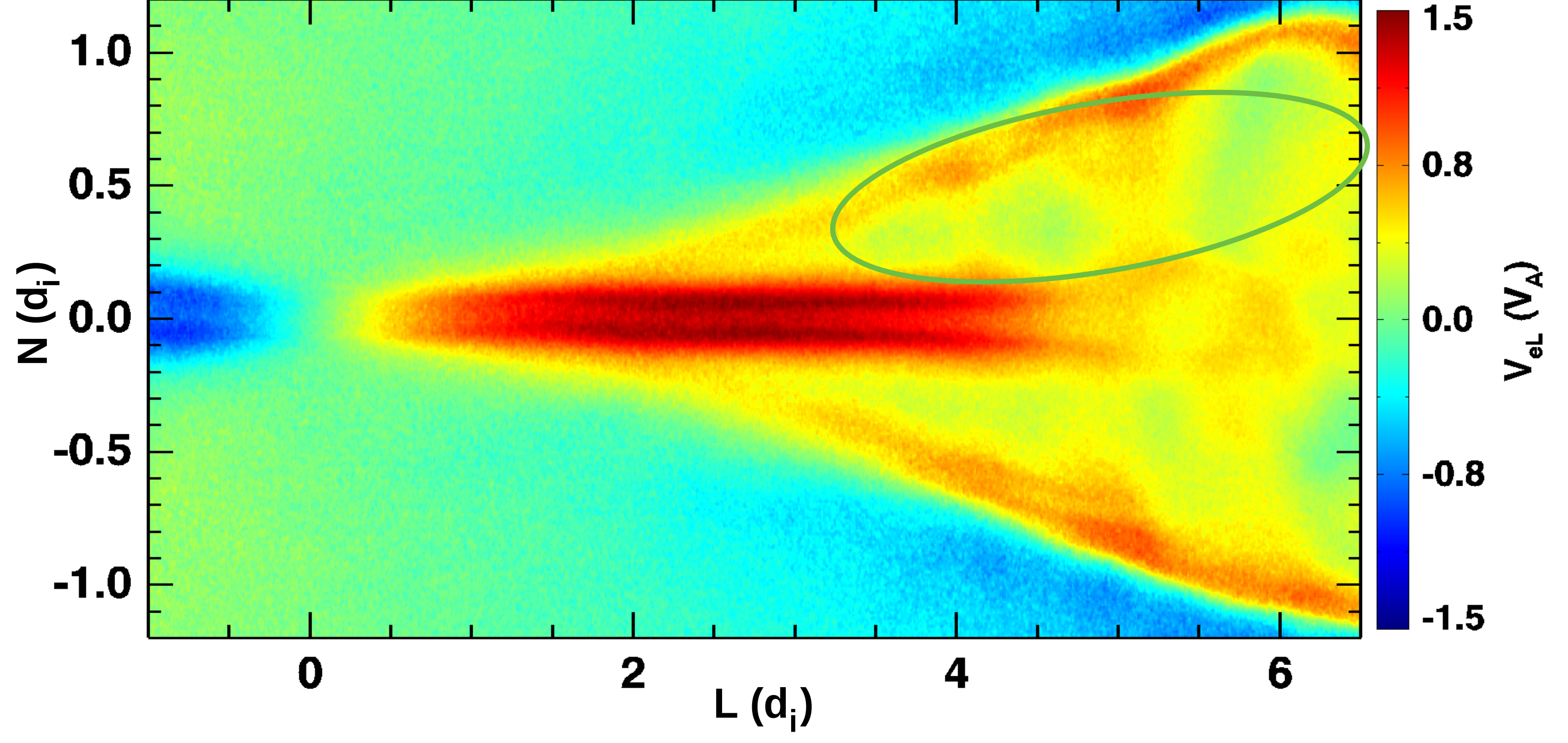

1.0
0.5
0.0
-0.5
-1.0
N (d$_i$)
0
2
4
6
L (d$_i$)
1.5
0.8
0.0
-0.8
-1.5
V$_{eL}$ (V$_A$)